



HAL
open science

Ice-rich (periglacial) vs icy (glacial) depressions in the Argyre region, Mars: a proposed cold-climate dichotomy of landforms

R.J. Soare, Susan J. Conway, C. Gallagher, J.M. Dohm

► To cite this version:

R.J. Soare, Susan J. Conway, C. Gallagher, J.M. Dohm. Ice-rich (periglacial) vs icy (glacial) depressions in the Argyre region, Mars: a proposed cold-climate dichotomy of landforms. *Icarus*, 2017, 282, pp.70-83. 10.1016/j.icarus.2016.09.009 . hal-02271715

HAL Id: hal-02271715

<https://hal.science/hal-02271715>

Submitted on 8 Jan 2021

HAL is a multi-disciplinary open access archive for the deposit and dissemination of scientific research documents, whether they are published or not. The documents may come from teaching and research institutions in France or abroad, or from public or private research centers.

L'archive ouverte pluridisciplinaire **HAL**, est destinée au dépôt et à la diffusion de documents scientifiques de niveau recherche, publiés ou non, émanant des établissements d'enseignement et de recherche français ou étrangers, des laboratoires publics ou privés.

1
2 | 02/08/2016 14:4802/08/2016 09:48
3
4
5
6

7 ***Ice-rich (periglacial) vs icy (glacial) depressions in the Argyre region, Mars:***
8 **a proposed cold-climate dichotomy of landforms**
9
10

11 R.J. Soare¹, S.J. Conway²⁻³, C. Gallagher⁴, J.M. Dohm⁵
12

13
14 ¹Department of Geography,
15 Dawson College, Montreal, Canada, H3Z 1A4
16 (rsoare@dawsoncollege.qc.ca)
17

18 ²Department of Physical Sciences,
19 Open University, Milton Keynes, United Kingdom, MK7 6AA
20

21 ³Laboratoire de Planétologie et Géodynamique - UMR CNRS 6112, 2 rue de la Houssinière -
22 BP 92208, 44322 Nantes Cedex 3, France.
23

24 ⁴UCD School of Geography, University College, Belfield, Dublin 4, Ireland

25 ⁵UCD Earth Institute, University College, Belfield, Dublin 4, Ireland
26

27 ⁶The University Museum, The University of Tokyo,
28 Hongo 7-3-1, Bunkyo-ku, Tokyo 113-0033, Japan
29

30
31
32 **Pages** - 32

33 **Figures** - 9

34 **Tables** - 2

35 **Keyword** - Mars, climate; Mars, surface; Mars, polar geology

36 **ABSTRACT**

37 On Mars, so-called “scalped depressions” are widely observed in Utopia Planitia (*UP*)
38 and Malea Planum (*MP*). Typically, they are rimless, metres- to decametres-deep, incised
39 sharply, tiered inwardly, polygonised and sometimes pitted. The depressions seemingly incise
40 terrain that is *icy* and possibly thermokarstic, i.e. produced by the thermal destabilisation of the
41 icy terrain. Age-wise, the depressions are thought to be relatively youthful, originating in the Late
42 Amazonian Epoch.

43 Here, we report the presence of similar depressions in the Argyre region (*AR*) (30-60⁰ S;
44 290-355⁰ E). more importantly, we separate and differentiate these landforms into two groups:
45 *ice-rich periglacial* depressions (Type-1); and, *icy glacial* depressions (Type-2a-c). This
46 differentiation is presented to the Mars community for the first time.

47 Based on a suite of morphological and geological characteristics synonymous with *ice-*
48 *complexes* in the Lena Peninsula (eastern Russia) and the Tuktoyaktuk Coastlands (Northwest
49 Territories, Canada), we propose that the Type-1 depressions are *ice-rich* periglacial basins that
50 have undergone volatile depletion largely by sublimation and as the result of thermal
51 destabilisation. In keeping with the terms and associated definitions derived of terrestrial
52 periglacial-geomorphology, *ice-rich* refers to permanently frozen-ground in which ice lenses or
53 segregation ice (collectively referenced as *excess ice*) have formed.

54 We suggest that the depressions are the product of a multi-step, cold-climate
55 geochronology:

- 56 1) Atmospheric precipitation and surface accumulation of an *icy* mantle during recent
57 high obliquities.

- 58 2) Regional or local triple-point conditions and thaw/evaporation of the mantle, either by
59 exogenic forcing, i.e. obliquity-driven rises of aerial and sub-aerial temperatures, or
60 endogenic forcing, i.e. along Argyre impact-related basement structures.
- 61 3) Meltwater migration into the regolith, at least to the full depth of the depressions.
- 62 4) Freeze-thaw cycling and the formation of *excess ice*.
- 63 5) Sublimation of the *excess ice* and depression formation as high obliquity dissipates
64 and near-surface ice becomes unstable.

65 The Type-2 depressions exhibit characteristics suggestive of *supra-glacial dead-ice*
66 *basins* and *snow/ice suncups* observed in high-alpine landscapes on Earth, e.g. the Swiss Alps
67 and the Himalayas. Like the Type-1 depressions, the Type-2 depressions could be the work of
68 sublimation; however, the latter differ from the former in that they seem to develop within a
69 glacial-like *icy* mantle that blankets the surface rather than within an *ice-rich* and periglacially-
70 revised regolith at/near the surface.

71 Interestingly, the Type-2 depressions overlie the Type-1 depressions at some locations. If
72 the periglacial/glacial morphological and stratigraphical dichotomy of depressions is valid, then
73 this points to recent glaciation at some locations within the *AR* being precursed by at least one
74 episode of periglaciation. This also suggests that periglaciation has a deeper history in the region
75 than has been thought hitherto. Moreover, if the hypothesised differences amongst the Argyre-
76 based depressions are mirrored in Utopia Planitia and Malea Planum, then perhaps this
77 periglacial-glacial dichotomy and its associated geochronology are as relevant to understanding
78 late period landscape-evolution in these two regions as it is in the *AR*.

79

80

81 1. Introduction

82 On Mars, depressions that are metre- to decametre-deep, polygonised (and sometimes
83 pitted) depressions that are rimless, incised sharply, inwardly-terraced or stepped, and
84 occasionally scalloped, are observed widely in Utopia Planitia (*UP*) (Costard and Kargel, 1995;
85 Seibert and Kargel, 2001; Morgenstern et al., 2007; Soare et al., 2007, 2008, 2009; Lefort et al.,
86 2009a; Séjourné et al., 2011, 2012; Ulrich et al., 2010) and Malea Planum (*MP*) (Lefort et al.,
87 2009b; Zanetti et al., 2010; Wilmes et al., 2012). The depressions are thought to: a) have formed
88 in the very Late Amazonian Epoch, given the sharpness of their incision, the highly-muted
89 terrain in which they occur, and sparse cratering; b) reside in *icy* terrain; and, c) be thermally
90 destabilised and ice-depleted - *thermokarstic* - as the result of near-surface and obliquity-driven
91 ice instability (Costard and Kargel, 1995; Morgenstern et al., 2007; Soare et al., 2007, 2008,
92 2009; Lefort et al., 2009a-b; Zanetti et al., 2010; Ulrich et al., 2010; Wilmes et al., 2012). Similar
93 depressions are observed in and around the Argyre impact-basin region (*AR*) in the southern
94 hemisphere (30-60⁰ S; 290-355⁰ E). Some workers suggest that this is a region where near-
95 surface water ice and surface liquid-water could be meta-stable even under current conditions
96 (Haberle et al., 2001; Zent et al., 1986, also, Hecht et al., 2002).

97 In the Lena Peninsula (eastern Russia) (e.g. Schirrmeister et al., 2002, 2013; Grosse et al.,
98 2007) and the Tuktoyaktuk Coastlands (Northwest Territories, Canada) (e.g. Washburn, 1973;
99 Mackay, 1979; Murton, 1996; Dallimore et al., 2000; Hill et al., 2001; French, 2007) depressions
100 of the type observed in the *AR*, as well in *UP* and *MP*, often occur in *ice-complexes*. These
101 complexes or landform assemblages are: *ice-rich* (i.e. containing *ice lenses* and *segregation ice*,
102 collectively reference as *excess ice*, from metres to decametres of depth); incised by ice-wedge
103 polygons and polygon trough/junction ponds or pits; punctuated by thermokarstic-terrain (i.e.

104 terrain underlain by excess ice) and rimless depressions or *alases* (where the excess ice has been
105 lost by evaporation or drainage) (e.g. Schirmer et al., 2002, 2013; Grosse et al., 2007).

106 Other depressions in the AR show morphologies and traits similar in some ways to those
107 presented above; however, they are distinguishable by the absence of polygonisation,
108 trough/junction pits and inward-oriented terraces and the presence of sharp rims (in some
109 instances), bowl-like shape and dense honeycomb-like clustering. Collectively, this second group
110 of depressions is suggestive of *supra-glacial lake basins* and of *snow/ice suncups* as observed,
111 for example, in the Swiss Alps (Kääb and Haeberli, 2001; Paul et al., 2007) and the Himalayas
112 (Benn et al., 2000; Reynolds, 2000).

113 *Supra-glacial lakes* occur in debris-covered *dead-ice* (ice that has been decoupled from
114 an originating glacier) (Kääb and Haeberli, 2001); here, irregularly-shaped crevasses formed by
115 the stress of glacial advance and retreat fill with water, derived of melted snow or ice, and evolve
116 into small metres-deep lakes that are metres to decametres in (long-axis) diameter (Kääb and
117 Haeberli, 2001). Meltwater drainage or evaporation exposes floor or basin morphologies similar
118 to those associated with the second group of Mars depressions. Small-sized polygons have not
119 been reported in the terrain adjacent to the *dead-ice lakes* or *basins* on Earth.

120 *Suncups* comprise sharply-narrow and sub-metre high ridges separated by smoothly-
121 concave sub-metre bowls or hollows (Betterton, 2001; Herzfeld et al., 2003); it is thought that
122 they form by the differentiated albeit highly-localised ablation (sublimation or evaporation) of
123 dirty vs clean snow (Betterton, 2001; Herzfeld et al., 2003; Mitchell and Tiedje, 2010).

124 In this article we have three main aims:

125 1) map the distribution of (**Fig. 1**) and describe the polygonised, tiered and sometimes-
126 pitted depressions in the AR, defined as Type-1 depressions (**Fig. 2**); discuss their

127 morphological and geological synonymy with the thermokarst terrain on Earth where *ice-*
128 *complexes* are observed (**Fig. 3**); and, propose a possible periglacial-origin for these
129 depressions.

130 2) map the distribution of (**Fig. 1**) and describe morphologically similar but
131 unpolygonised, untiered and unpitted Type-2 depressions in the region (**Fig. 4**); we
132 propose that these depressions are glacial in origin and analogous to alpine *dead-ice lake*
133 basins and *suncups* on Earth (**Fig. 5**).

134 3) hypothesise that an endogenic influence could be responsible, at least in part, for the
135 thermal de-stabilisation required to form the Type-1 depressions.

136 Numerous studies have explored the possibility of freeze-thaw cycling of water affecting
137 landscape changes throughout the *AR* during the Late Amazonian Epoch: a) clastically sorted,
138 small-sized ($\leq \sim 25$ m in diameter) polygons (Banks et al., 2008; Soare et al., 2016); b) clastically
139 unsorted, small-sized and low-centred polygons (Soare et al., 2014a); c) (possible) hydraulic or
140 open-system pingos (Soare et al., 2014b); and, d) gelifluction-like lobes (Johnsson et al., 2015;
141 Soare et al., 2015, 2016). The proposed dichotomy of landforms and associated geochronology
142 presented here is consistent with this premise and underlines the extent to which relatively-recent
143 boundary conditions in the *AR* might have been less uniformly cold and dry, perhaps even to the
144 present day, than is generally thought.

145 **2. Definition of key periglacial terms**

146 The proposed differentiation of periglacial from glacial depressions in the Argyre region
147 can be meaningful only in as much as the key referential or framing terms are identified and then
148 defined clearly. Towards this end, the generally-accepted usage of these terms in terrestrial
149 geology and periglacial-geomorphology is our benchmark. We recognise that some workers in
150 the Mars community of planetary scientists believe that the relevance and viability of definitions

151 derived of terrestrial systems or landscapes is contingent upon their adaptation to the Martian
152 context (e.g. Byrne et al., 2009; Dundas et al., 2015; Sizemore et al., 2015). However, until a
153 discrete and thorough discussion on appropriate periglacial-terms and -definitions for Mars
154 appears in the scholarly literature, deference to the current lexicon of terrestrial geology and
155 periglacial-geomorphology might be the most prudent course to plot.

156 **2.1 Permafrost and excess ice**

157 *Permafrost*, i.e. soil that has been frozen for at least two years, is *ice-rich* if and when it
158 contains *excess ice* (Harris et al. 1988). *Excess ice* describes *permafrost* those pore space is
159 exceeded by ice within that body; it comprises discrete *ice lenses* or lenses of *segregation ice*
160 that range in thickness from hairline to >10m and, typically, are observed in alternating horizons
161 of ice and soil (Penner, 1959; Harris et al., 1988). Fine-grained soils are particularly adept at
162 forming *excess ice* because their small pores and pathways induce the movement of unfrozen
163 water to the freezing front at a rate commensurable with the formation of *ice lenses* (Penner,
164 1959; Harris et al., 1988). Frost settlement or deflation occurs when *excess ice* thaws and
165 meltwater pools or is removed from the thaw site is lost by evaporation or drainage (Washburn,
166 1973; French, 2007).

167 **2.2 Thermokarst**

168 Generically, terrain that comprises *ice-rich* permafrost and, is subject to frost settlement
169 or deflation is referenced as *thermokarst* (e.g. Washburn, 1973, Harris et al. 1988, Murton, 1996;
170 Dallimore et al., 2000; French, 2007) (**Fig. 3a**). An *alas* is the depression formed by the
171 surface/near-surface and localised loss of *excess ice* (Harris et al., 1988). If this loss produces a
172 pond and, subsequently, if the ponded water evaporates or drains episodically, inwardly-oriented
173 and scalloped-shaped benches or terraces may develop on the basin margins (**Fig. 3b**).

174 The shape (sub-circular to elongate), size (metres to kilometres in long-axis diameter),
175 depth (sub- to multi-metres) and distribution (individually, clustered or coalesced) of
176 *thermocarst* landforms mirror the vertical and horizontal distribution of *ice-rich permafrost* in a
177 landscape and the penetration reach of a thermal wave (e.g. Washburn, 1973, Harris et al. 1988,
178 Murton, 1996; French, 2007). Terrain punctuated by the presence of *excess ice* is particularly
179 sensitive to disturbance and volumetric loss if or when seasonal or annual mean-temperatures
180 rise substantially (e.g. Washburn, 1973; Mackay, 1992; Hill et al., 2001; French, 2007).

181 **2.3 Thermal-contraction polygons**

182 Often, *thermocarstic* terrain is incised by small-sized (generally ≤ 25 m in diameter) and
183 non-sorted (thermal-contraction) polygons (e.g. Mackay, 1972, 1992; Rampton, 1988; Hill et al.,
184 2001; Kääh and Haeberli, 2001) (**Fig. 3b-f**). Thermal-contraction fracturing is the result of
185 tensile stresses in frozen ground induced by the sharp drop of sub-zero (0°C) temperatures
186 (Lachenbruch, 1962; Harris et al., 1988). Thermal-contraction fractures or cracks neither entail
187 nor require the availability of liquid water (Lachenbruch, 1962). However, ice wedges and
188 eventually, ice-wedge polygons, may form in thermal-contraction cracks when, where and when
189 surface-meltwater migrates and freezes *in situ*.

190 If these ice wedges thaw, meltwater may pool and then pond within the marginal troughs
191 and junctions that bound the polygons (**Figs. 3c-f**). Impelled by thermal erosion, the ponds
192 sometimes grow and evolve into small-scale fluvio-lacustrine systems or streams that have a
193 beaded appearance (**Figs. 3d**) (e.g. Hopkins et al., 1955; Washburn, 1973; Black, 1976; Harris et
194 al., 1988; French, 2007). They are beaded, as melt-water pools more substantially at polygon
195 junctions than within polygon troughs, and systemic, in as much as the polygon troughs connect

196 or link individual pools or beads to one another (Washburn, 1973; Harris et al., 1988; French,
197 2007).

198 **3. Methods**

199 In order to identify possible mantle-incising periglacial and glacial depressions within the
200 *AR*, we performed a systematic survey of the available HiRISE (High Resolution Imaging
201 Science Experiment) images (n=1044) that cover the region (30-60°S; 290-355°E) (**Fig. 6**). We
202 excluded depressions that present characteristics consistent with impact craters, i.e. completely
203 circular with a raised rim (whether ejecta were present or not). HiRISE images are between 25
204 and 50 cm/pix; they have sufficient resolution to identify the geological context of these
205 depressions. One of the key-observations that motivated our wider survey was that the
206 depressions seemingly show different morphologies depending on whether or not they are
207 spatially associated with polygonally-patterned ground. The presence or absence of metre-scale
208 polygonally patterned ground can be ascertained with confidence only at the resolution of
209 HiRISE images. Therefore, although many of the depressions included in this study are visible in
210 Mars Orbiter Camera, Narrow Angle (MOC-NA; ~1.5 m/pix) or Mars Reconnaissance Orbiter
211 Context (CTX; 6 m/pix) images, the associated features cannot be identified; hence they are not
212 encompassed in this study.

213 We use two methods to estimate depression depths. One or the other method was
214 employed in an opportunistic fashion when the data were available. Firstly, where the
215 depressions are large enough (at least twice the Mars Orbiter Laser Altimeter (MOLA) shot-
216 spacing, ~300 m) and if they are also crossed by MOLA tracks, these cross sections are used to
217 estimate depression depth, as follows. We fit a plane to the points on either side of the depression
218 (or on one side if both sides were not made of the same material) and measure the maximum

219 vertical-distance between this plane and the MOLA shot located at the lowest elevation within
 220 the depression. Secondly, where the depressions are small we use shadow measurements to
 221 estimate depression depths; however, because such depressions have very shallowly-sloping
 222 walls we perform this analysis only where images are taken with high solar-incidence angles.

223 Shadow measurements are performed according to the method presented in (Dauber et
 224 al., 2014). Briefly, shadows cast by depression walls are measured along the solar azimuth on the
 225 RDR HiRISE image and then converted to height (h) by assuming a flat-floored depression and
 226 then applying the following formula: $h = l_m / \sqrt{(\tan^2 i + \tan^2 e - 2 \tan i \tan e \cos v)}$ where l_m is the
 227 measured length, i is the incidence angle, e is the emission angle and v is the subsolar azimuth. It
 228 should be noted that for the majority of the images surveyed, we were not able to apply either of
 229 these methods, because of the limitations of these methods, mentioned above.

230 **4. Observations**

231 ***4.1 Type-1 depressions***

232 Of the 1044 HiRISE images that cover the AR we report twenty-five locations where the
 233 Type-1 depressions are observed (**Fig. 1; Table 1**). These locations overlie thirteen disparate
 234 geological-units that range in age from the late Noachian to the late Hesperian Epochs. Six of the
 235 fourteen locations (cf. Table 1, # 14-15, 17-20) are ($\sim 48.8\text{-}55.6^\circ\text{S}$; $297.5\text{-}307.5^\circ\text{E}$) are amidst or
 236 adjacent to a geological corridor linking Argyre Planitia to a large basin on its western flank in
 237 the cratered highlands. Dohm et al. (2015) refer to this basin as the Argyre western-margin
 238 paleolake (*AWMP*). Here, linear margins and tectonic structures are widespread; this points to
 239 the possibility of impact-related basement-control of the surface geology (Dohm et al., 2015).
 240 Otherwise, the distribution of the Type-1 depressions shows no apparent latitudinal-constraint or

241 gradient as one would expect were obliquity-driven climate the dominant control of depression
242 formation (**Fig. 1; Table 1**).

243 The Type-1 depressions (**Fig. 2a-h**) display various plan-forms: circular (**Fig. 2b**) or sub-
244 circular (**Fig. 2c-d**), tear-dropped (**Fig. 2f**) and, occasionally, scalloped, exhibiting inward-
245 oriented tiers or terraces (**Fig. 2d**). They are observed individually (**Fig. 2b**), clustered (**Fig. 2c-**
246 **d**) or coalesced, sometimes in wave-like (planform) patterns of distribution (**Fig. 2e**).
247 Depression-length (long axes of the depressions defined by the outermost closed-contour line)
248 ranges from ~85-1000 m; widths range from ~50-500 m. Depression-depths reach ~40m (**Figs.**
249 **7a-b**); however, it should be noted that we are able to identify only two sites where the
250 depressions are significantly larger than the MOLA shot spacing and are crossed by MOLA
251 tracks. Collectively, we ascertain no preferred geographical-orientation amongst individual
252 depressions, although this could be an artefact of the small sample-size. However, where the
253 depressions coalesce, each of them display the same (long-axis) orientation (**e.g. Figs. 2c-d**).
254 Depression margins are continuous albeit rimless, well defined and, often, relatively sharp (**Figs.**
255 **2c-d**). Generally, depression floors are sloped gently and their gain or loss of elevation follows
256 the local topography (**Figs. 7a-b**). Some floors, however, are uneven and are covered in part by
257 rocky debris and boulders (**Fig. 2c**).

258 In all of the Type-1 depressions identified by us, depression-margins, -sides, -floors and
259 even the terrain beyond the depressions themselves, are incised by small-sized (~5 m) and non-
260 sorted polygons (**e.g. Figs. 2b-g; cf. Table 1**). Many of these polygons comprise centres
261 surrounded by marginal metre to sub-metre (diameter) troughs and trough-junctions (**Fig. 2g**).
262 Some of the intra-depression polygonal troughs and junctions are pitted (**Fig. 2g**). These pits are
263 circular to sub-circular and measure a metre or more in diameter (**Fig. 2g**). Where the pits are

264 slightly larger than this, the shape of the underlying troughs and/or junctions is distorted, even
265 obscured (**Fig. 2g**).

266 Some pits are connected; this gives them the appearance of linked beads (**Fig. 2g**).
267 Occasionally, the connected pits display metre-wide and fan-like features that overtop the trough
268 margins (**Fig. 2h**). Overall, there seems to be no uniform orientation of pit or trough alignment;
269 both north-south (or south-north) (**Fig. 2g**) and west-east (or east-west) orientation (**Fig 2g**) are
270 commonplace, although as noted above with regard to the Type-1 depressions themselves, this
271 could be an artefact of the small sample-size. Where the pits and cavities are clustered, the
272 surrounding terrain may form a slight depression (**Fig. 2g**).

273 Typically, the depressions are embedded in a smooth (and relatively light-toned) mantle
274 that mutes the underlying terrain and topography (**Fig. 8a**). Mantle depth ranges from metres to
275 decametres (**Figs. 7a-b**). Impact craters are sparse and boulders/rocky terrain are scarce where
276 the mantle is continuous and relatively thick. Where the depression-dissected mantle is
277 discontinuous and relatively thin, rocky terrain may be observed adjacent to the mantle. The
278 latter, invariably, exhibits no depressions (**Fig. 8b**). At some locations the polygonised Type-1
279 mantle seemingly underlies the Type-2 mantle (**Fig. 4f**).

280 *4.2 Type 2 depressions*

281 Overall, the observed Type-2(a-c) depressions are more numerous than the Type-1
282 depressions and are located largely to the north of 50⁰ S (**Fig. 1; Table 2**). The Type-2(a)
283 depressions are decametre to kilometre in scale and copy the diverse morphology of Type-1
284 depressions (**Figs. 4a-c**), except for the absence of scalloped rims, tiered interior slopes, wave-
285 like planform or interior polygonal-patterning.

286 Like the Type-1 depressions, the Type-2(a) depressions are rimless; they are also
287 anchored in mantled terrain that is relatively smooth (**Figs. 4b, d-e**), cratered sparsely and absent
288 of boulders/rocky terrain; however, unlike the Type-1 depressions, neither the 2(a) depressions
289 nor the terrain incised by them are polygonised at any of the locations observed by us (**Figs. 4a-**
290 **c**).

291 Type-2(b) depressions comprise multi-metre to decametre-scale pits that are shaped
292 irregularly and rimmed sharply (**Figs. 4c-d, f**). These pits or hollows occur in dense clusters that
293 exhibit a honeycomb-like appearance and, often, reside within Type-2(a) depressions. The 2(b)
294 depressions, like the 2(a) depressions, show smooth textures that are not polygonised. As noted
295 in the previous section, some Type-2(b) depressions and the Type-2 mantle incised by them
296 appear to overlie a Type-1 mantle, the latter being identified by its polygonisation (**Fig. 4f**).

297 The Type-2(c) depressions, similarly to the 2(b) depressions, are shaped irregularly, have
298 raised-rims and display diameters in the multi-metre to decametre range (**Figs. 4g-h**). Where the
299 distribution of these depressions is dense and ubiquitous, as it may be throughout the inter-crater
300 plains of the region, the depressions impart a sponge-like texture to the landscape (**Figs. 4g-h**).
301 The ubiquity of these depressions enables us to estimate their depths using shadow-
302 measurements on low sun-angle images. For Table 2-location 22 (ESP_026851_1445, solar
303 incidence 76.7°) we made 100 random measurements of shadows cast by the walls of the
304 depressions; depression depths range from 0.5-4.7m and the average depth is 2.3 m (**Fig. 9a**). For
305 Table 2-location 27 (ESP_028552_1440, solar incidence 66.892612°) we made 30 random
306 measurements; depression depths range from 0.6-3.2 m and the average depth is ~ 1.6 m (**Fig.**
307 **9b**). The Type-2(c) depressions are observed on impact-crater ejecta (**Fig. 4i**); terrain adjacent to
308 the ejecta (**Fig. 4i**); and, as noted above, expansively on inter-crater terrain.

309 **4.3 Type-1 depressions: uniquely different from Type-2 depressions**

310 In the main, there are five key traits or characteristics that differentiate the Type-2(a-c)
311 from the Type-1 depressions. First, the Type-1 depressions are polygonised, as is the terrain
312 adjacent to the depressions; by means of contrast, the Type-2 depressions are unpolygonised in
313 all observed instances, as is the terrain adjacent to them. Second, the Type-1 depressions exhibit
314 pitting, sometimes beaded, within polygon-margin troughs and trough-junctions. Pitting of this
315 type is not observed in conjunction with any of the Type-2 depressions. Third, some of the Type-
316 1 depressions, especially those that exhibit wave-like clustering, are scalloped and show inward-
317 oriented tiers or terraces; none of the observed Type-2 depressions exhibit similar traits. Fourth,
318 the bowl-like and multi- to decametre-wide Type-2(b) depressions often are nested within the
319 Type-2(a) depressions but never within the Type-1 depressions. Fifth, where the Type-2 and
320 Type-1 mantles (and their spatially-associated depressions) are observed concurrently in a
321 landscape the Type-1 mantle underlies the Type-2 mantle in all instances.

322 **5. Type-1 depressions and possible ice-rich (periglacial) complexes**

323 The spatial-synonymy of the Type-1 depressions and the (sometimes) pitted, (invariably)
324 polygonised-terrain in the Argyre region (within and adjacent to the Type-1 depressions) mirrors
325 that of thermokarst/alas assemblages and polygon-margin pits in periglacial, *ice -rich complexes*
326 on Earth. As noted above, the latter develop a) when and if *excess ice* is present in the near-
327 surface permafrost, sometimes to decametres of depth; and, b) when and if the *excess ice*
328 undergoes heat-induced thermal destabilisation and is removed from the permafrost by
329 evaporation or drainage.

330 The possible origin and loss of *excess ice* as a precursive condition to the formation of
331 Type-1 depressions is neither simple nor straightforward. In order to frame our hypothesis aptly,

332 we propose a (simplified) four-step meteorological and geological chronology. It coalesces
333 generally-accepted assumptions concerning obliquity-related *icy* mantle formation in the Late
334 Amazonian Epoch with the requirements of forming an *ice-complex* derived of freeze-thaw
335 cycles in periglacial landscapes on Earth. *Ice complexes* formed entirely by means of vapour-
336 diffusion cycles have yet to be observed on Earth.

337 (Step-1): A water- or dusty-ice mantle forms at the mid to high latitudes of both
338 hemispheres; it is the obliquity-driven product of atmospheric precipitation and surface
339 accumulation (e.g. Mustard et al., 2001; Milliken et al., 2003; Head et al., 2003, 2006; Tanaka et
340 al., 2005; Forget et al., 2006; Madeleine et al., 2009, 2014; Schorghofer and Forget, 2012). This
341 mantle predates the very Late Amazonian Epoch mantle commonly referenced in the literature
342 by these and other workers but would be consistent with the origin, composition, landscape
343 characteristics and geographical distribution of the current mantle discussed by them.

344 The observed and deduced evidence favouring an *icy* composition for the later mantle in
345 the *AR* is as follows: (1) the elevated occurrence of near-surface water ice (inferred from the
346 Mars Odyssey gamma-ray and neutron-spectrometer data); (2) landforms whose morphology
347 collectively implies a glacial landscape, i.e. moraine- and esker-like ridges, lobate-debris aprons
348 (i.e. possible debris covered rock-glaciers) and semi-circular (cirque-like) embayments; (3) the
349 latitudinal constraint/distribution of the observed mantled-terrain, predicted by models linking
350 ground-ice stability with recent changes in the obliquity and spin parameters of Mars (Banks et
351 al., 2008, 2009; Wilmes et al., 2010; Zanetti et al., 2012; El Maarry et al., 2013).

352 (Step-2): As Mars moves towards high obliquity the early or antecedent mantle thaws and
353 generates meltwater, especially in areas such as the *AR* where water could be metastable even
354 under current conditions (e.g. Haberle et al., 2001; Zent et al., 1986; also, see Hecht, 2002);

355 mantle thaw also could be produced endogenically were deeply-seated heat to be delivered to the
356 surface by means of Argyre (impact-related) geothermal pathways, identified by linear margins
357 and tectonic structures at the surface (Dohm et al., 2015; Williams et al., 2016; also, Soare et al.,
358 2014).

359 (Step-3): The meltwater migrates into the underlying fine-grained regolith (Soare et al.,
360 2016) and undergoes episodic freeze-thaw iterations at discrete and disparate freezing-fronts.
361 This forms multiple *ice lenses* or layers. Basaltic regolith, thought to be commonplace in the AR
362 (e.g. Bandfield and Rogers, 2008), would be an ideal medium for this type of preferential freeze-
363 thaw cycling and the formation of *excess ice*.

364 (Step-4): The ice degrades or ablates, probably by sublimation, as high obliquity wanes
365 (e.g. Morgenstern et al., 2007; Lefort et al., 2009a-b; Séjourné et al., 2011, 2012) or in response
366 to highly-localised endogenic forcing (Dohm et al., 2015); alas-like Type-1 depressions are
367 formed. Subsequently, thermal-contraction cracking polygonises the depressions and the
368 surrounding terrain (Costard and Kargel, 1995; Seibert and Kargel, 2001; Mangold et al., 2005;
369 Levy et al., 2009). In turn, small-scale pits and linked beaded-troughs form within polygon
370 margins; this could be the work of near-surface ice being removed from the regolith by
371 sublimation or thaw/evaporation (Wan Bun Tseung and Soare, 2006; Soare et al., 2008; Séjourné
372 et al., 2010; 2011, 2012).

373 **6. Type-2 depressions and a high-alpine (glacial) analogue**

374 A follow-up cycle of *icy* mantle-formation and -degradation occurs in the more recent
375 past. As the mantle forms it blankets the terrain in which the polygonised Type-1 depressions
376 developed and subsequently, at an indeterminately later time, begins to sublimate; dead-ice (like)
377 basins and snow/ice suncups are an end-product of this sublimation (Massé et al., 2010;

378 Mangold, 2011). Further degradation ablates the mantle sufficiently to expose the underlying
379 Type-1 depressions, as well as the polygonised terrain that incises and encompasses them.

380 **7. Discussion and conclusion**

381 On the basis of disparate morphological-traits, trait-assemblages and landscape-
382 characteristics we have identified two different depression-types (Type-1 and Type-2) in the AR.
383 We propose that the first depression-type approximates (periglacial) *alases* on Earth, whereas the
384 second type exhibits striking similarities with terrestrial (supra-glacial) *dead-ice basins* and
385 *suncups*.

386 The glacial pathway that produces the Type-2 depressions is somewhat simpler than the
387 one associated with the periglacial formation of the Type-1 depressions; it is also largely
388 consistent with the widely-held beliefs about obliquity-driven mantle formation and degradation
389 in the Late Amazonian Epoch. Moreover, the plausibility of the glacial pathway is not contingent
390 upon triple-point conditions being reached.

391 By means of contrast, the periglacial pathway that engenders the formation of the Type-2
392 depressions requires multiple episodes of freeze-thaw cycling (perhaps facilitated by the
393 presence of brines in the regolith), antecedent mantle-formation and -degradation, and the
394 accumulation of *excess ice* to decametres of depth.

395 Some preliminary work has explored a possible formation-pathway for near-surface *ice*
396 *lenses* and *excess ice* based on absorption/diffusion cycles (Dundas, 2015; Sizemore, 2015).
397 However, whether this pathway is robust enough to form excess ice to the depths associated with
398 the largest of the Type-1 (alas-like) depressions is an open question.

399 The observed superposition of the Type-2 mantle and associated depressions on
400 polygonised Type-1 terrain suggests that discrete and multiple episodes of relatively-recent

401 mantle formation can be identified, separated stratigraphically, and linked to disparate cold-
402 climate origins. It also highlights the possibility that significant thermokarstic-revisions of the
403 regional landscape in the *AR* predate the most recent period of glaciation.

404 Interestingly, some of the Type-1 depressions exhibit polygon-junction and trough-pitting
405 as well as some small-scale beading comprised of interconnected polygon-junction and polygon-
406 trough pits. Similar morphologies are observed in *ice-rich* landscapes on Earth and are diagnostic
407 of: a) antecedent polygonised ice-wedging; b) ice thaw; c) the formation, ponded accumulation
408 and eventual evacuation of ice-derived meltwater by evaporation or drainage; and, d) the
409 organisation of localised fluvio-lacustrine (periglacial) systems. At some locations small fan-like
410 features overtop the beaded troughs; this points to the possibility of highly-localised debris flow.

411 The relative absence of uniformity in the orientation of the junction-pit linked-
412 assemblages argues against the possibility of formation by aeolian deflation (Morgenstern et al.,
413 2007; Séjourné et al., 2010) or by tectonic/structural forces (Lefort et al., 2009a). But even if the
414 pits and beading are the work of sublimation, not evaporation or drainage, the morphologies of
415 the pits and beads points strongly towards the presence of near-surface ground-ice, a key marker
416 of an ice-rich landscape.

417 The absence of an apparent latitudinal-constraint on the distribution of the Type-1
418 depressions, as well as the paucity of the Type-1 depressions compared to the Type-2
419 depressions, is enigmatic. Under current or recent aerial or sub-aerial boundary conditions, ice
420 stability is thought to increase with latitude (e.g. Mellon and Jakosky, 1995; Head et al., 2003;
421 Morgenstern et al., 2007; Lefort et al., 2009b; Zanetti et al., 2010; Dundas, 2015). If the
422 ascription of a thermokarstic origin to the Type-1 depressions is valid, then one would expect the
423 number of Type-1 depressions to decrease with latitude, in line with an increase of ice stability.

424 On the other hand, the small number of observed Type-1 depressions could be the result
425 of highly-localised and favourable surface-pressures and temperatures in the *AR* when the
426 depressions formed, as could be inferred from Haberle et al., (2001) and Zent et al., (1986), also
427 Hecht (2002).

428 An endogenic origin of thermal instability ought not to be discounted either. A few Type-
429 1 depressions are clustered in the area of the *AWMP*. Here, linear margins and tectonic structures
430 are widespread and, as noted above, some recent work has hypothesised a connexion between
431 deeply-seated heat, possible impact-related geothermal pathways and ice instability at/near the
432 surface in this and other areas of the *AR* (Dohm et al., 2015; Williams et al., 2016; also, Soare et
433 al., 2014).

434 Lastly, the surface coverage of the Argyre impact-basin floor by the *HiRISE* imagery is
435 poor and small in scale. Perhaps the small population of observed Type-1 depressions is simply
436 an artefact of this poor coverage.

437 However, were the presumed differences between the two depression-types in the *AR*
438 valid and mirrored in Utopia Planitia and Malea Planum, then perhaps the commonly-held belief
439 that the *UP* and *MP* depressions are rooted directly in an *icy* mantle ought to be revisited.

440 **References**

- 441 Bandfield, J.L., Rogers, A.D., 2008. Olivine dissolution by acidic fluids in Argyre Planitia,
442 Mars: evidence for a widespread process? *Geology* 36, 7, 579-582,
443 doi:10.1130/G24724A.1.
- 444 Banks, M.E., et al., 2008. High resolution imaging science experiment (HiRISE) of glacial and
445 periglacial morphologies in the circum-Argyre Planitia highlands, Mars. *Journal of*
446 *Geophysical Research* 113, E12015, doi:10.1029/2007JE002994.

- 447 Benn, D.I., Wiseman, S., Warren, C.R., 2000. Rapid growth of a supraglacial lake, Ngozumpa
448 Glacier, Khumbu Himal, Nepal, in Nakawo, M., Raymond, C.F., and Fountain, A., (eds.).
449 Debris-Covered Glaciers, IAHS publication 264, 177-185.
- 450 Betterton, M.D., 2001. Theory of the structure formation in snowfields motivated by penitentes,
451 suncups, and dirt cones. *Physical Review E*, 63, 056129, 1-12, doi:10.1103/PhysRevE.63.
452 056129.
- 453 Black, R.F., 1976. Features indicative of permafrost. *Annual Review of Earth and Planetary
454 Sciences* 4, 75-94.
- 455 Byrne, S. et al., 2009. Distribution of mid-latitude ground ice on Mars from new impact craters.
456 *Science* 325, 5948, 1674-1676, doi:10.1126/science.1175307.
- 457 Costard, F.M., Kargel, J.S., 1995. Outwash plains and thermokarst on Mars. *Icarus* 114, 1, 93-
458 112, doi:10.1006/icar.1995.1046.
- 459 Dallimore, A., Schröder-Adams, C.J., Dallimore, S.R. 2000. Holocene environmental history of
460 thermokarst lakes on Richards Island, Northwest Territories, Canada: thecamoebians as
461 paleolimnological indicators. *Journal of Paleolimnology* 23, 261-283.
- 462 Dauber, I.J., Atwood-Stone, C., Byrne, S., McEwen, A.S., Russell, P.S., 2014. The morphology
463 of small fresh craters on Mars and the Moon. *Journal of Geophysical Research: Planets*
464 119, 2014JE004671, doi:10.1002/2014JE004671
- 465 Dohm, J.M., et al., 2015. Geological and hydrological histories of the Argyre Province, Mars,
466 253, 66-98 *Icarus* doi:10.1016/j.icarus.2015.02.017.
- 467 Dundas, C., Byrne, S., McEwen, A.S., 2015. Modeling the development of Martian sublimation
468 thermokarst landforms. *Icarus* 262, 154-169, dx.doi.org/10.1016/j.icarus.2015.07.033
- 469 Federov, A.N., Gavrilev, P.P., Konstantinov, P.Y., Hiyama, T., Iijima, Y., Iwahana, G., 2014.

- 470 Estimating the water balance of a thermokarst lake in the middle of the Lena River basin,
471 eastern Siberia. *Ecohydrology* 7, 188-196, doi:10.1002/eco.1378.
- 472 Forget, F., Haberle, R.M., Montmessin, D., Levrard, B., Head, J.W., 2006. Formation of
473 glaciers on Mars by atmospheric precipitation at high obliquity. *Science* 311, 368,
474 doi:10.1126/ science/1120335.
- 475 French, H.M., 2007. *The periglacial environment*, 3rd ed., J. Wiley & Sons, West Sussex,
476 England, 458 p.
- 477 Grosse, G., Schirmer, L., Siegert L., Kunitsky, V.K., Slagoda, E.A., Andreev, A.A.,
478 Dereviagn, A.Y., 2007. Geological and geomorphological evolution of a sedimentary
479 periglacial landscape in Northeast Siberia during the Late Quaternary. *Geomorphology*
480 86, 25-51.
- 481 Haberle, R.M., McKay, C.P., Schaeffer, J., Cabrol, N., Grin, E.A., Zent, A.P., Quinn, R. 2001.
482 On the possibility of liquid water on present day Mars. *Journal of Geophysical Research*
483 106, E10, 23,317-23,326.
- 484 Harris, S.A., French, H.M., Heginbottom, J.A., Johnston, G.H., Ladanyi, B., Sego, D.C., van
485 Everdingen, R.O., (eds.), 1988. *Glossary of permafrost and related ground-ice terms*.
486 Technical Memorandum 142, Permafrost Subcommittee, National Research Council of
487 Canada, 154 p.
- 488 Head, J.W., Mustard, J.F., Kreslavsky, M.A., Milliken, R.E., Marchant, D.R., 2003. Recent
489 ice ages on Mars. *Nature* 426, 797-802, doi:10.1038/nature02114.
- 490 Head, J.W., Marchant, D.R., Agnew, M.C., Fassett, C.I., Kreslavsky, M.A., 2006. Extensive

- 491 valley glacier deposits in the northern mid-latitudes of Mars: Evidence for Late
492 Amazonian obliquity-driven climate change. *Earth and Planetary Science Letters* 241,
493 663-671, doi:10.1016/j.epsl.2005.11.016.
- 494 Hecht, M.H., 2002. Metastability of liquid water on Mars. *Icarus* 156, 373-286, doi:10.1006/icar.
495 2001.6794.
- 496 Herzfeld, U.C., Mayer, H., Caine, N., Losleben, M., Erbrecht, T., 2003. Morphogenesis of
497 typical winter and summer snow surface patterns in a continental alpine environment.
498 *Hydrological Processes* 17, 619-649, doi:10.1002/hyp.1158.
- 499 Hill, P.R., Lewis, C.P., Desmarais, S., Kauppaymuthoo, V., Rais., H., 2001. The Mackenzie
500 Delta: sedimentary processes and facies of a high-latitude, fine-grained delta.
501 *Sedimentology* 48, 1047-1078.
- 502 Hopkins, D.M., Karlstrom, T.N.V., Black, R.F., Williams, J.R., Péwé, T.L., Fernold, A.T.,
503 Muller, E.H., 1955. Permafrost and ground water in Alaska, a shorter contribution to
504 general geology; a study of the interrelations of permafrost and ground water, and a
505 discussion of the role of aerial photographs in the mapping and evaluation of permafrost
506 conditions. Geological Survey Professional Paper 264-F, Washington, D.C., United
507 States Government Printing Office, 70 p.
- 508 <http://www.ultralight backpacker.com/index.html>, Joe's ultralight backpacking.
- 509 Johnsson, A., Reiss, D., Conway, S.J., Hauber, E., Hiesinger, H., 2015. Small-scale lobes in the
510 southern hemisphere on Mars: implications for transient liquid water in the recent past.
511 European Planetary Science Congress, Nantes, France, 10, 882.
- 512 Käab, A., Haeberli, W., 2001. Evolution of a high mountain thermokarst lake in the Swiss Alps.
513 *Arctic, Antarctic and Alpine Research* 33, 4, 385-390.

- 514 Lachenbruch, A.H., 1962. GSA Special Paper 70. Geological Society of America, New York,
515 69p.
- 516 Lefort, A., Russell, P.S., McEwen, A.S., Dundas, C.M., Kirk, R.L., 2009a. Observations of
517 periglacial landforms in Utopia Planitia with the High Resolution Imaging Science
518 Experiment (HiRISE). *Journal of Geophysical Research* 114, E04005, doi:10.1029/
519 2008JE003264.
- 520 Lefort, A., Russell, P.S., Thomas, N., 2009b. Scalloped terrains in the Peneus and Amphrities
521 Paterae of Mars as observed by HiRISE. *Icarus* 205, 1, 259-268, doi:10.1016/j.icarus.
522 2009.06.005.
- 523 Levy, J., Head, J.W, Marchant, D.R., 2009. Thermal contraction crack polygons on Mars:
524 Classification, distribution and climatic implications from HiRISE observations. *Journal*
525 *of Geophysical Research* 114, E01007, doi:10.1029/2008JE003273.
- 526 Mackay, J.R., 1972. The world of underground ice. *Annals of the Association of American*
527 *Geographers* 62, 1, 1-22.
- 528 Mackay, J., 1979. Pingos of the Tuktoyaktuk Peninsula, Northwest Territories, *Géographie*
529 *physique et quaternaire* 33, 1, 3-61.
- 530 Mackay, J.R., 1992. Lake stability in an ice-rich permafrost environment: examples from the
531 western Arctic coast. In R. D. Robarts & M. L. Bothwell (eds), *Aquatic Ecosystems in*
532 *Semi-arid Regions: Implications for Resource Management*. N.H.R.I. Symposium Series
533 7, Environment Canada, Saskatoon, Canada, 1–22.
- 534 Madeleine, J-B., Forget, F., Head, J.W., Levrard, B., Montmessin, F., Millour, E., 2009.
535 Amazonian northern mid-latitude glaciation on Mars: a proposed climate scenario. *Icarus*
536 203, 390-405, dx.doi.org/10.1016/j.icarus.2009.04.037.

- 537 Madeleine, J-B., Head, J.W., Forget, F., Navarro, T., Millour, E., Spiga, A., Colaitis, A.,
538 Määttänen, A., Montmessin, F., Dickson, J.L., 2014. Recent Ice Ages on Mars: The role
539 of radiatively active clouds and cloud microphysics. *Geophysical Research Letters* 41,
540 14, 4873-4879, doi:10.1002/2014GL059861.
- 541 Mangold, N. 2005. High latitude patterned grounds on Mars: classification, distribution and
542 climatic control. *Icarus* 174, 336-359, doi:10.1016/j.icarus.2004.07.30.
- 543 Mangold, N., 2011. Ice sublimation as a geomorphic process: a planetary perspective.
544 *Geomorphology* 126, 1-17, doi:10.1015/geomorph.2010.11.009.
- 545 Massé, M., Bourgeois, O., Le Mouélic, S., Verpoorter, C., Le Deit, L., Bibring, J.P., 2010.
546 Martian polar and circum-polar sulfate-bearing deposits: sublimation tills derived from
547 the North Polar Cap. *Icarus*, 209, 2, 434-451, doi:10.1016/j.icarus.2010.04.017.
- 548 Mellon, M., Jakosky, B.M., 1995. The distribution and behavior of martian ground ice during
549 past and present epochs. *Journal of Geophysical Research* 100, E6, 11781-11799.
- 550 Milliken, R.E., Mustard, J.F., Goldsby, D.L., 2003. Viscous flow features on the surface of
551 Mars: Observations from high-resolution Mars Orbiter Camera (MOC) images. *Journal*
552 *of Geophysical Research* 108, E6, 5057, doi:10.1029/2002JE002005.
- 553 Mitchell, K.A., Tiedje, T., 2010. Growth and fluctuations of suncups on alpine snowpacks.
554 *Journal of Geophysical Research* 115, F04039, doi:10.1029/2010JF001724.
- 555 Morgenstern, A., Hauber, E., Reiss, D., van Gasselt, S., Grosse, G., Schirrmeyer, L., 2007.
556 Deposition and degradation of a volatile-rich layer in Utopia Planitia, and implications
557 for climate history on Mars. *Journal of Geophysical Research* 112, E06010, doi:10.1029/
558 2006JE002869.
- 559 Murton, J., 1996. Thermokarst-lake basin sediments, Tuktoyaktuk Coastlands, western arctic

- 560 Canada. *Sedimentology* 43, 737-760.
- 561 Mustard, J.F., Cooper, C.D., Rifkin, M.R., 2001. Evidence for recent climate change on Mars
562 from the identification of youthful near-surface ground ice. *Nature* 412, 411-414. doi:10.
563 1038/35086515.
- 564 Paul, F., Kääb, A., Haeberli, W., 2007. Recent changes in the Alps observed by satellite:
565 consequences for future monitoring strategies. *Global and Planetary Change* 56, 111-122.
- 566 Penner E., 1959. The mechanism of frost heaving in soils. Highway Research Board, Bulletin
567 225, 1-22.
- 568 Rampton, V.N., 1988. Quaternary Geology of the Tuktoyaktuk Coastlands, Northwest
569 Territories, Geological Survey of Canada, Memoir 423, 98 p.
- 570 Reynolds, J.M., 2000. On the formation of supraglacial lakes on debris-covered glaciers, in
571 Nakawo, M., Raymond, C.F., and Fountain, A., (eds.). *Debris-Covered Glaciers*, IAHS
572 publication 264, 153-164.
- 573 Robbins, S.J., Hynek, B.M., 2012. A new global data base of Mars impact craters ≥ 1 km.
574 Database creation, properties, and parameters. *Journal of Geophysical Research* 117, E5,
575 doi:10.1029/2011JE003966.
- 576 Robbins, S.J., Hynek, B.M., Lillis, R.J., Bottke, W.F., 2013. Large impact crater histories of
577 Mars: the effect of different model crater age techniques. *Icarus* 225, 173-184, doi.org/10.
578 1016/j.icarus.2013.03.01.
- 579 Schirrmester, L., Siegert, C., Kunitszky, V.V., Grootes, P.M., Erlenkeuser, H., 2002. Late
580 Quaternary ice-rich permafrost sequences as a paleoenvironmental archive for the Laptev
581 Sea Region in northern Siberia. *International Journal of Earth Sciences* 91, 154-167.
- 582 Schirrmester, L., Froese, D., Tumskey, V., Grosse, G., Wetterich, S., 2013. Yedoma: Late

- 583 Pleistocene ice-rich syngenetic permafrost of Beringia, in, Elias., S.A., (ed.) The
584 Encyclopaedia of Quaternary Science 3, 542-552. Amsterdam: Elsevier.
- 585 Schorghofer, N., Forget, F., 2012. History and anatomy of subsurface ice on Mars. *Icarus* 220,
586 1112-1120, doi:10.1016/j.icarus.2012.07.003.
- 587 Seibert, N.M., Kargel, J.S., 2001. Small-scale martian polygonal terrain: implications for liquid
588 surface water. *Geophysical Research Letters* 28, 5, 899-902.
- 589 Séjourné, A., Costard, F., Gargani, J., Soare, R.J., Marmo, C., 2010. The polygon junction pits as
590 evidence of a particularly ice-rich area in Utopia Planitia, 41st Lunar and Planetary
591 Science Conference, Houston, Texas, 2113.
- 592 Séjourné, A., Costard, F., Gargani, J., Soare, R.J., Fedorov, A., Marmo, C., 2011. Scalloped
593 depressions and small-sized polygons in western Utopia Planitia: a new formation
594 hypothesis. *Planetary and Space Science* 59, 412-422, doi:10.1016/j.pss.2011.01.007.
- 595 Séjourné, A., Costard, F.N., Gargani, J., Soare, R.J., Marmo, C., 2012. Evidence of an eolian ice-
596 rich and stratified permafrost in Utopia Planitia, Mars. *Planetary and Space Science* 60,
597 348-254, doi:10.1016/j.pss.2011.09.004.
- 598 Sizemore, H.G., Zent, A.P., Rempel, A.W., 2015. Initiation and growth of Martian ice lenses.
599 *Icarus* 251, 191-210, doi:org/10.1016/j.icarus.2014.04.013.
- 600 Soare, R.J., Kargel, J.S., Osinski, G.R., Costard, F., 2007. Gully formation, periglacial processes
601 and evidence of near-surface ground-ice in Utopia and western Elysium Planitia. *Icarus*
602 191, 1, 95-112, doi:10.1016/j.icarus.2007.04.018.
- 603 Soare, R.J., Osinski, G.R., Roehm, C.L., 2008. Thermokarst lakes and ponds on Mars in the very
604 recent (late Amazonian) past. *Earth and Planetary Science Letters* 272, 1-2, 382-393,
605 doi:10.1016/j.epsl.2008.05.10.

- 606 Soare, R.J., Osinski, G.R., 2009. Stratigraphical evidence of late Amazonian periglaciation and
607 glaciation in the Astapus Colles region of Mars. *Icarus* 202, 1. 17-21. doi:10.1016/j.
608 icarus.2009.02.009.
- 609 Soare, R.J., Séjourné, A., Pearce, G., Costard, F., Osinski, G.R., 2011. The Tuktoyaktuk
610 Coastlands of northern Canada: A possible “wet” periglacial analogue of Utopia
611 Planitia, Mars. In: Garry, W.B., Bleacher, J.E. (Eds.), *Analogs for Planetary Exploration*.
612 Geological Society of America Special Paper 483. doi:10.1130/2011.2483(13).
- 613 Soare, R.J., Conway, S.J., Séjourné, A., Dohm, J.M., 2012. Climate change & the origin of ice-
614 rich permafrost in mid Utopia Planitia, Mars. Mars Recent Climate Change Workshop,
615 NASA Ames Research Centre, Moffett Field California. Abstract #
- 616 Soare, R.J., Conway, S.J., Dohm, J.M., 2014a. Possible ice-wedge polygons and recent
617 landscape modification by “wet” periglacial processes in and around the Argyre impact
618 basin, Mars. *Icarus* 233, 214-228, doi.org/10.1016/j.icarus.2014.01.034.
- 619 Soare, R.J., Conway, S.J., Dohm, J.M., El-Maarry, M.R., 2014b. Possible open-system
620 (hydraulic) pingos in and around the Argyre impact region of Mars. *Earth and Planetary*
621 *Science Letters* 398, 25-36, doi:10.1016/j.epsl.2014.04.044.
- 622 Soare, R.J., Horgan, B., Conway, S.J., Souness, C., El-Maarry-M.R., 2015. Volcanic terrain and
623 the possible periglacial formation of “excess ice” at the mid-latitudes of Utopia Planitia,
624 Mars. *Earth and Planetary Science Letters* 423, 182-192, doi.org/10.1016/j.epsl.2015.04.
625 033
- 626 Soare, R.J., Conway, S.J., Gallagher, C., Dohm, J.M., 2016. Sorted (clastic) polygons in the
627 Argyre region, Mars, and possible evidence of pre- and post-glacial periglaciation in the
628 Late Amazonian Epoch. *Icarus* 264, 184-197, doi:10.1016/j.icarus.2015.09.019.

- 629 Ulrich, M., Morgenstern, A., Günther, F., Reiss, D., Bauch, K.E. Hauber, E., Rössler, S.,
630 Schirrmeister, L., 2010. Thermokarst in Siberian ice-rich permafrost: Comparison to
631 asymmetric scalloped depressions on Mars. *Journal of Geophysical Research* 115,
632 E10009, doi:10.1029/2010JE003640.
- 633 Wan Bun Tseung, J.M., Soare, R.J., 2006. 37th Lunar and Planetary Science Conference,
634 Houston, Texas, 1414.
- 635 Washburn, A.L., 1973. *Periglacial processes and environment*. New York, NY, St Martin's
636 Press, 320 p.
- 637 Williams, J.P., Pathare, A., Dohm, J.M., Lopes, R.M.C., Buczkowski, D.L., 2016. Volcanism
638 and giant polygons within the Argyre Basin, Mars, 47th Lunar and Planetary Science
639 Conference, Abstract 2423.
- 640 Wilmes, M., Reiss, D., Hiesinger, H., Zanetti, M., 2012. Surface age of the ice-dust mantle
641 deposit in Malea Planum, Mars. *Planetary and Space Science*, 60, 199-206, dx.doi.org/
642 1016/j.pss.2011.08.006.
- 643 Zanetti, M., Hiesinger, H., Reiss, Hauber, E., Neukum, G., 2010. Distribution and evolution of
644 scalloped terrain in the southern hemisphere, Mars. *Icarus* 206, 691-706, doi:10.1016/j.
645 icarus.2009.09.010.
- 646 Zent, A.P., Fanale, F.P., Salvail, J.R., Postawko, S.E., 1986. Distribution and state of H₂O in the
647 high-latitude shallow subsurface of Mars, *Icarus*, 67, 19-36.

648 **Acknowledgements**

649 RJS thanks Dawson College, in particular, D. Gauvin and L. Bennett, for a professional
650 development leave that enabled him to present some of the ideas in this article precursively at the
651 Nantes EPSC in October, 2015.

652 **Figures**

653 **Fig. 1**

654 Geological-unit map of the Argyre impact-crater and surrounding region of Mars
 655 (adapted from Dohm et al., 2015). The global geological-map is shown for areas outside
 656 of the Dohm et al. (2015) map. Type-1 depressions highlighted in orange; Type-2
 657 depressions (shown in Fig. 4) highlighted in pink.

658 **Fig. 2**

659 **(a)** Type-1 (depression) morphologies and distribution (context-image). **(b)** Circular
 660 depression. Note the polygonised terrain surrounding the depression and the polygonised
 661 depression-walls and -floors. **(c)** Four coalesced (sub-circular) depressions. Note the E/W
 662 or W/E latitudinal orientation of their collective long axes. **(d)** Sub-circular depressions
 663 that exhibit coalescence, scalloping and some wave-like (planform) distribution **(e)**
 664 Coalesced depressions with more extensive wave-like distribution **(a-e:** HiRISE image
 665 ESP_011319_1305; 298.954⁰E, 49.001⁰S; res. 50cm/pixel; NASA/JPL/University of
 666 Arizona). **(f)** Tear-drop shaped depression with longitudinally-orientated long-axis
 667 (HiRISE image ESP_013890_1240; 307.523⁰E, 55.615⁰S; res. 50cm/pixel;
 668 NASA/JPL/University of Arizona). **(g)** Depression with pitted and deformed polygon-
 669 margin troughs and junctions. Note the clustering and branching of these features
 670 (HiRISE image PSP_006176_1225.323.637⁰E, 57.130⁰S; res. 50cm/pixel;
 671 NASA/JPL/University of Arizona). **(h)** Polygon troughs with N/S orientation overtopped
 672 by small fan-like structures (HiRISE image PSP_006176_1225).

673 **Fig. 3**

674 **(a)** Thermokarst lake/alas (light-coloured and unvegetated patches of terrain)
 675 assemblages in the Tuktoyaktuk Coastlands. **(b)** Archetypal recession of a thermokarst-
 676 lake margin and the associated scalloping of that margin. **(c)** Thermokarst lake/alas

677 assemblage. Note, 1. the receding lake-margin (top-left corner) and the subsequential
 678 polygonisation of the newly exposed lake-basin floor; and 2. the formation of a beaded
 679 fluvial-channel that meanders through interconnected polygon-margins at the right flank
 680 of the thermokarst lake. **(d)** Development of landscape-wide fluvial systems by means of
 681 interconnected polygon-troughs. **(e)** Small-scale pooling of meltwater at polygon margins
 682 on alas floors. **(f)** Convergence of pools and the formation of meltwater ponds. All air-
 683 photos are of the Tuktoyaktuk Coastlands (Northwest Territories, Canada) between
 684 Inuvik and Tuktoyaktuk. Image credits: R. Soare.

685 **Fig. 4**

686 **(a-c)** Type 2(a) depressions: circular, sub-circular and tear-dropped; rimless; and,
 687 decametres hundreds of metres in diameter (HiRISE images ESP_038785_1390;
 688 334.041° E, 40.881° S; res. 25 cm/pixel; PSP_007824_1420; 322.026° E, 37.895° S; res.
 689 50cm/pixel; ESP_021734_1460; 353.240° E, 33.752° S; 25 cm/pixel;
 690 NASA/JPL/University of Arizona). **(d, also c, f)** Type 2(b) depressions: smaller scale
 691 than Type 2(a), rimmed and, often, clustered densely on the floor and walls of the latter
 692 ESP_021734_1460; 353.240° E, 33.752° S; 25 cm/pixel; NASA/JPL/University of
 693 Arizona). **(e, also b, d, f)** Type 2 lightly-toned and mantled-terrain. Note the absence of
 694 cratering and the mutedness of the underlying topography (HiRISE image
 695 PSP_007824_1420; 322.026° E, 37.895° S; res. 50 cm/pixel; NASA/JPL/University of
 696 Arizona). **(f)** Type 2(a) depression incised by multiple Type 2(b) depressions, both of
 697 which overlie a Type 1 depression (as marked by the dark-toned and polygonised strip of
 698 terrain on the left-hand side of the image). Here the Type-2 mantle seemingly has
 699 contracted, possibly ablated, and revealed the underlying dark-toned Type-1 terrain that
 700 might not be visible otherwise (HiRISE image PSP_007033_1445; 321.183° , E 35.000°

701 S; 50 cm/pixel; NASA/JPL/University of Arizona). **(g-h)** Type 2(c) depressions: possible
 702 example of mantle degradation, with (g) showing less degradation than (h) (HiRISE
 703 images ESP_028552_1440; 339.485⁰, E 35.640⁰ S; 50cm/pixel; ESP_026851_1445;
 704 333.395⁰, E 35.002⁰ S; 25 cm/pixel; NASA/JPL/University of Arizona). **(i)** Type 2(c)
 705 depressions on the ejecta of an impact crater (HiRISE image ESP_022315_1440;
 706 330.846⁰, E 35.843⁰ S; 25 cm/pixel; NASA/JPL/University of Arizona).

707 **Fig. 5**

708 Glacial (dead-ice) thermokarst-lake set in glacial debris/overburden (basin area =
 709 ~10,000m²; the height of the ice-front to the left is >10m (Kääb and Haeberli, 2001;
 710 copyright by the Regents of the University of Colorado). Here, lake formation is
 711 triggered by thaw. We hypothesise that morphologically similar dead-ice features, i.e.
 712 thermokarst basins, could have formed in the AR by means of ice-sublimation. **(b)** Alpine
 713 suncups (Mather Pass, California). Image credit: [http://www.ultralight](http://www.ultralightbackpacker.com/index.html)
 714 [backpacker.com/index.html](http://www.ultralightbackpacker.com/index.html).

715 **Fig. 6**

716 Overview of the HiRISE images surveyed and the sites identified with Type-1 and Type-
 717 2 depressions. Background THEMIS-Day IR Global mosaic from ASU. The geographic
 718 locations of Figs. 2, 4, 7 and 8 and their sub-figures are shown and labelled in black.

719 **Fig. 7**

720 Topographic profiles of Type-1 depressions with context images. On each topographic
 721 profile the black points are Mars Orbiter Laser Altimeter (MOLA) shots; the grey lines
 722 are linear interpolations across the depressions, using the three points adjacent to the
 723 depression boundary (excluding obvious non-mantled hills). Labels give the maximum

724 distance between the interpolated line and the MOLA data. **(a)** CTX image
 725 B17_016132_1327_XN_47S061W with superposed MOLA shot points (in purple)
 726 obtained from the PDS; the outline of HiRISE image ESP_011319_1305 (in red) at site 6
 727 and the locations of the topographic profiles shown below (in black). **(b)** CTX image
 728 P15_007033_1429_XN_37S038W with superposed MOLA shot points (in purple)
 729 obtained from the PDS; the outline of HiRISE images ESP_016197_1445 and
 730 PSP_007033_1445 (in red) at site 1; and, the locations of the topographic profiles shown
 731 below (in black).

732 **Fig. 8**


733 **(a)** Mid-latitude valley floor covered by terrain that is smooth, i.e. mantled, albeit
 734 lineated; boulders are sparse (ESP_013890_1240; 307.523⁰E, 55.615⁰S; res. 50 cm/pixel;
 735 NASA/JPL/University of Arizona). **(b)** Mid-latitude mantled terrain in Charitum
 736 Montes; note the relatively steep and abrupt change of elevation where the putative
 737 mantle ends and the rocky terrain begins (ESP_032628_1275; 300.048⁰E, 52.398⁰S; res.
 738 50 cm/pixel; NASA/JPL/University of Arizona).


739 **Fig. 9**

740 **(a)** HiRISE image ESP_026851_1445 (Table 2-location 22, solar incidence 76.7°), red
 741 crosses mark the locations where we made 100 random measurements of shadows cast by
 742 the walls of the Type-2c depressions. **(b)** HiRISE image ESP_028552_1440 (Table 2-
 743 location 27, solar incidence 66.892612°), red crosses mark the locations where 30
 744 random measurements are made.

Figure


Legend


 Type 1 depressions

 Type 2 depressions


Geological Units

Amazonian/Hesperian

 AHTp, Thaumasia plateau SE

 HAB4a, Argyre basin member 4a


Hesperian/Noachian


 HNH4, Highlands member 4


 HNH3, Highlands member 3

 HNTTh, Thaumasia highlands


Noachian

 NAb4b, Argyre basin member 4b

 NAb3, Argyre basin member 3


 NAb2, Argyre basin member 2

 NAb1, Argyre basin member 1

 NArsp, Argyre rim smooth plains materials

 NAbr, Argyre basin and rim materials

 NArb, Argyre rim and basin materials

 NAr, Argyre rim materials


 Nh2, Highlands member 2

 Nh1, Highlands member 1

 Nhb, Highlands basins materials

Crater Units

 Cfr, Rough crater floor materials

 Cfs, Smooth crater floor materials

 C2, Young crater materials

 C1, Old crater materials

Global Geology

Polar Units

 Hp

Basin Units

 mNhm

 HNb

Highland Units

 mNh

 lNh

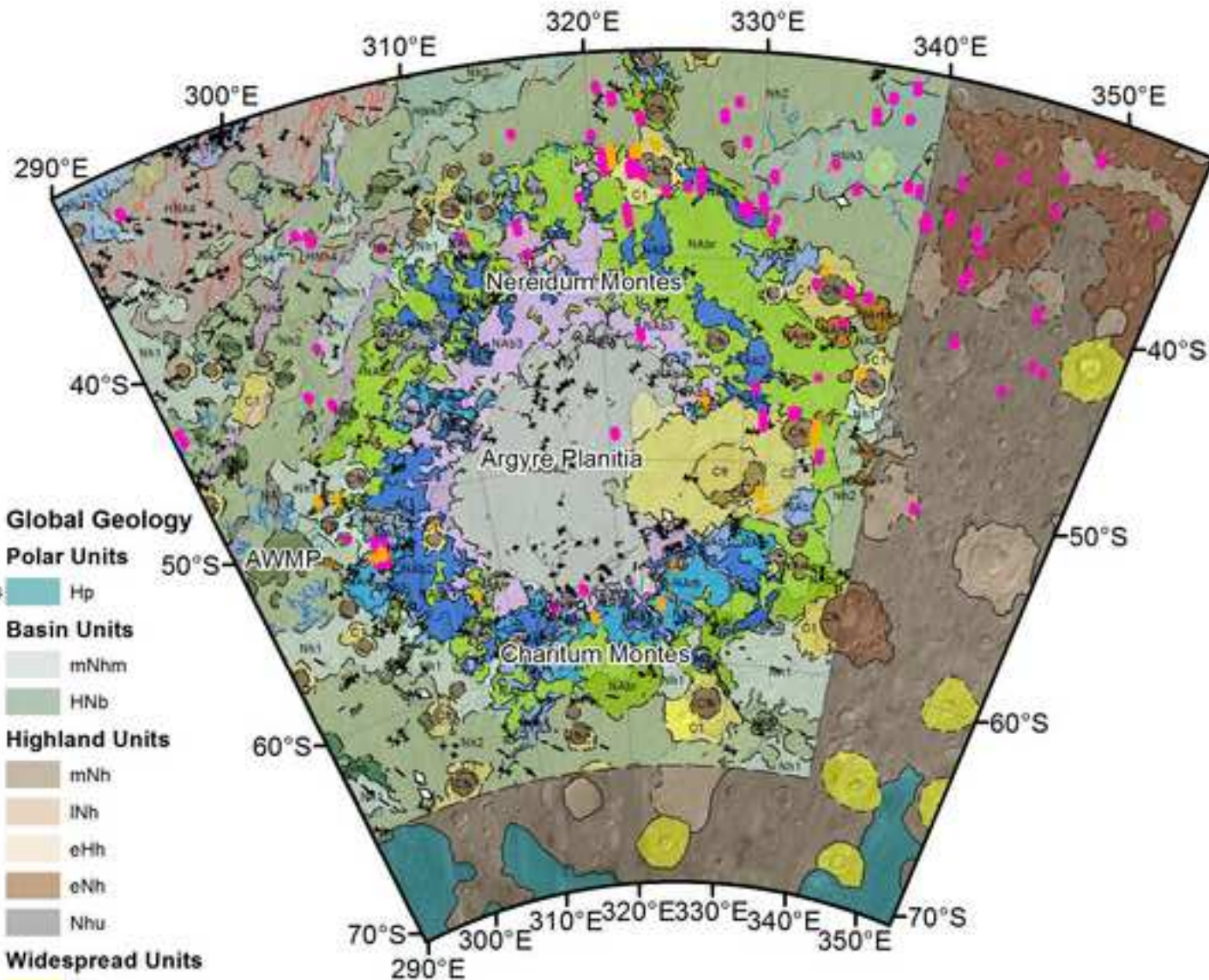
 eHh

 eNh

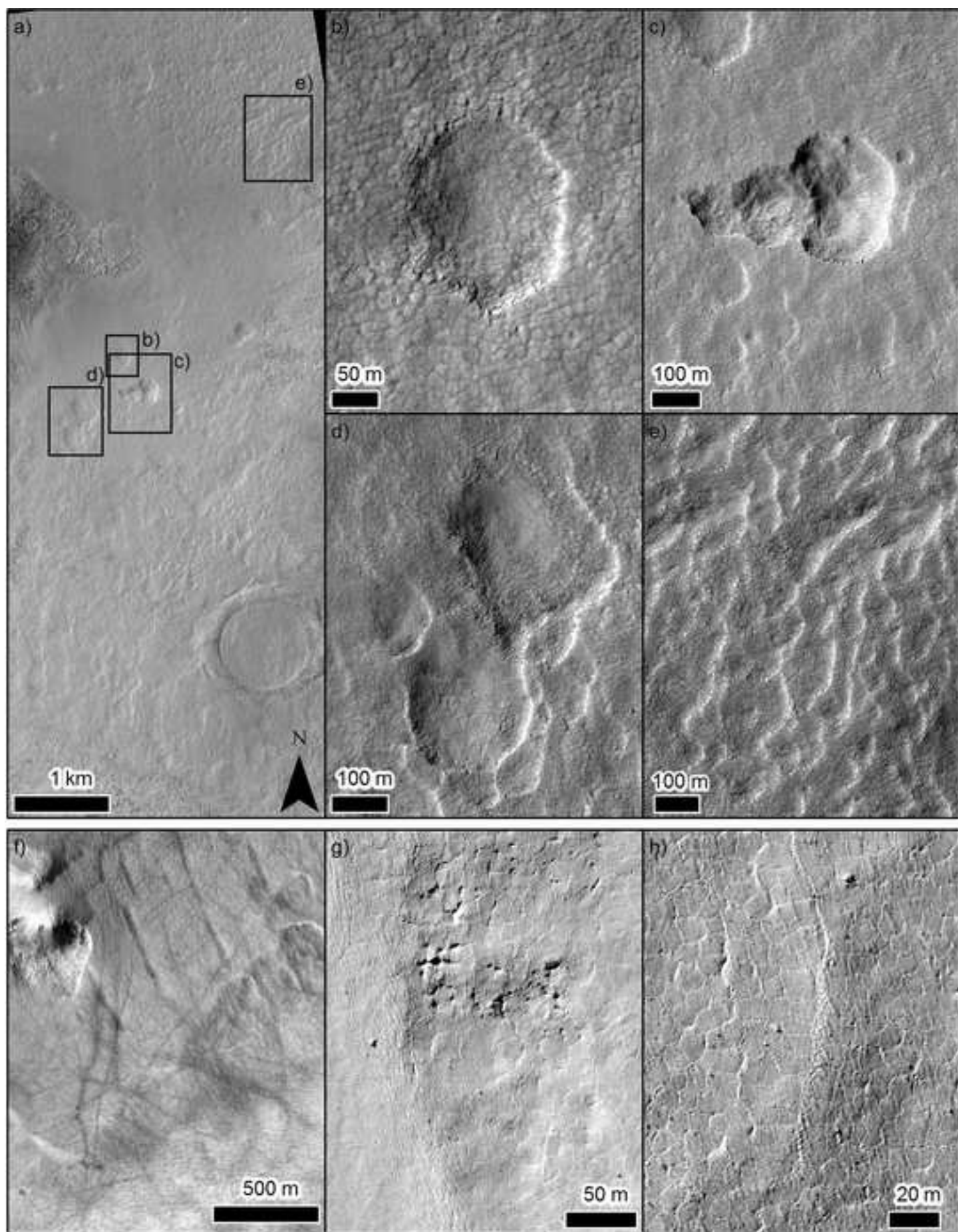
 Nhu

Widespread Units

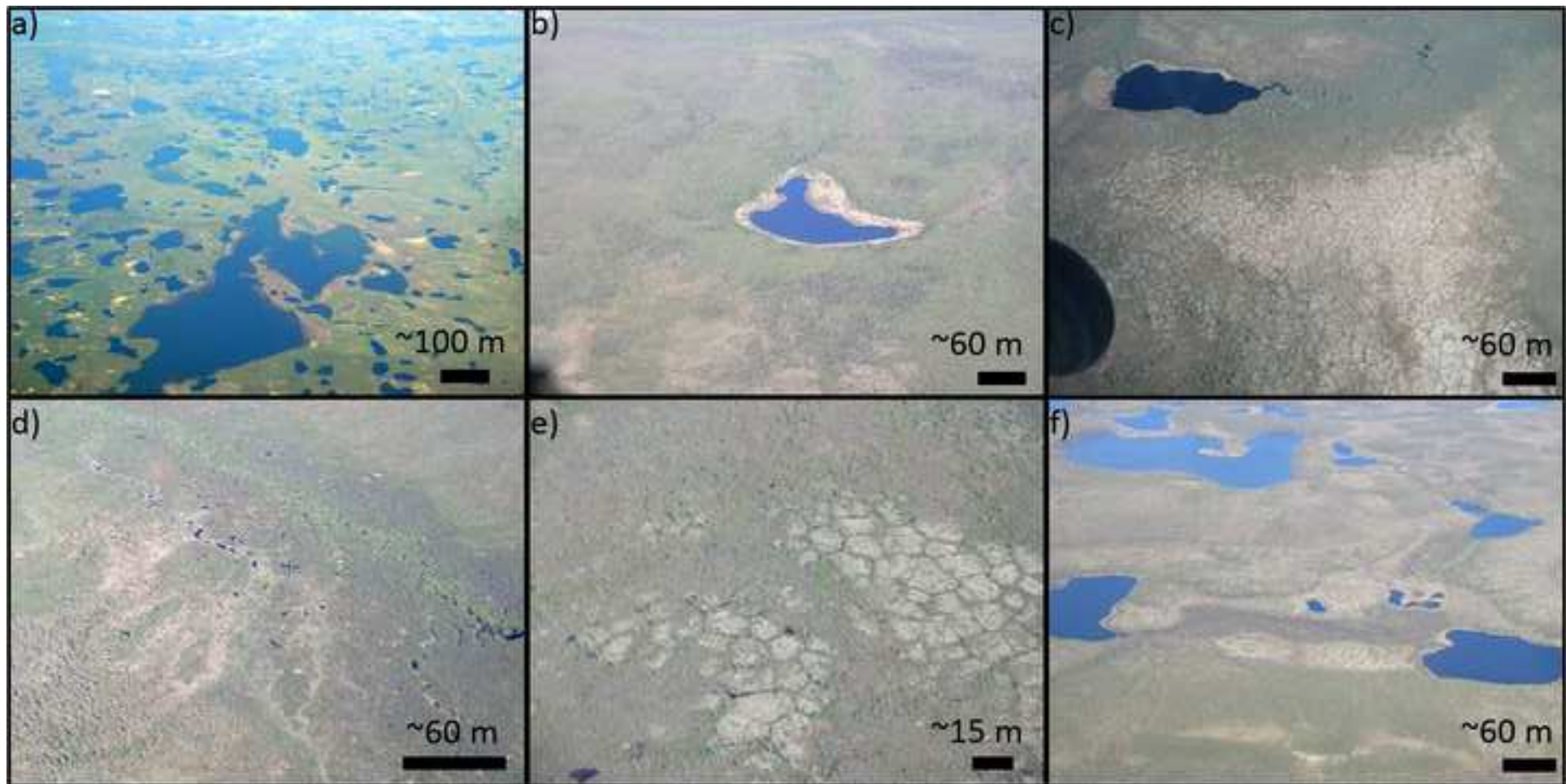
 AHi



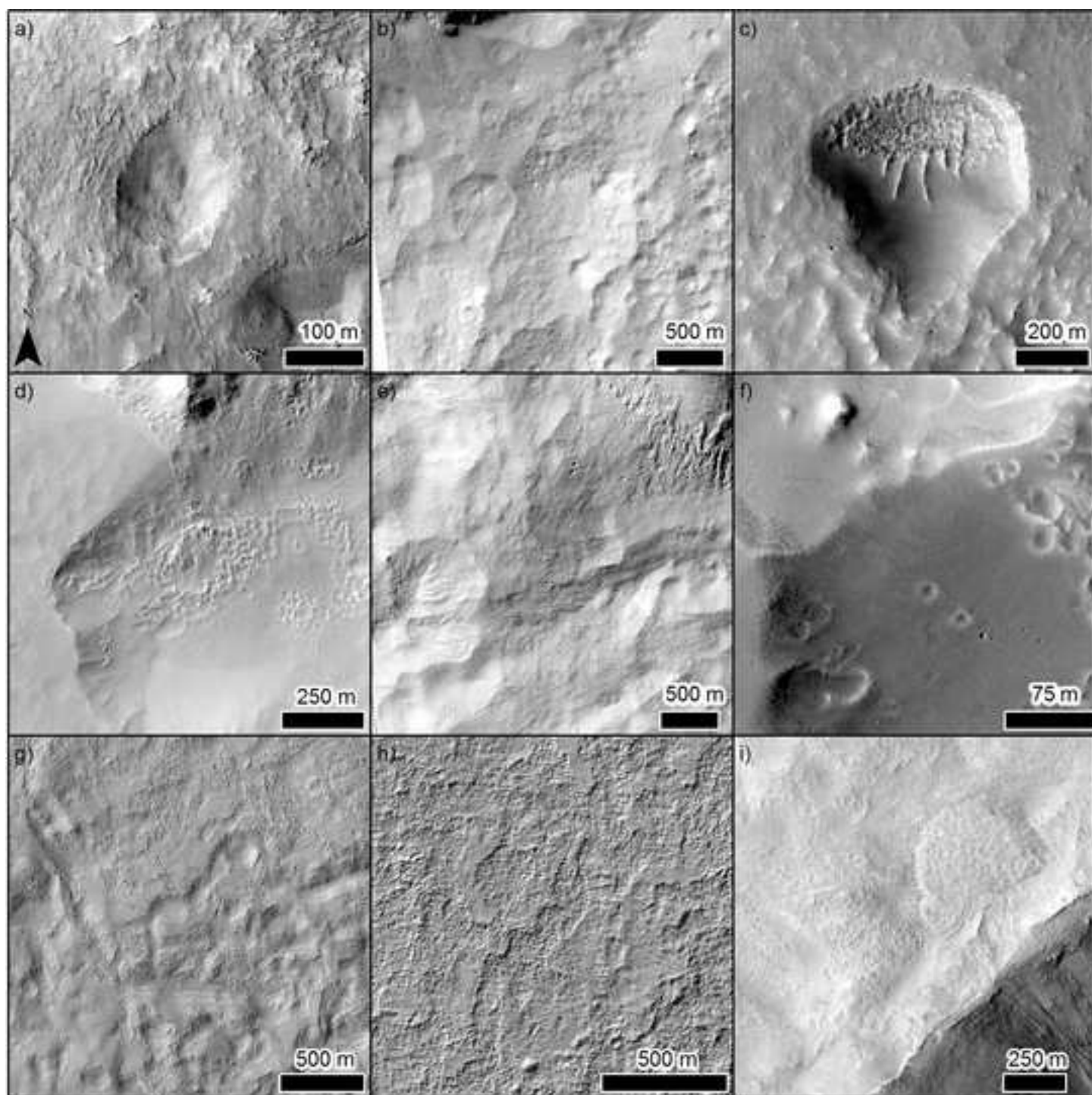
Figure



Figure



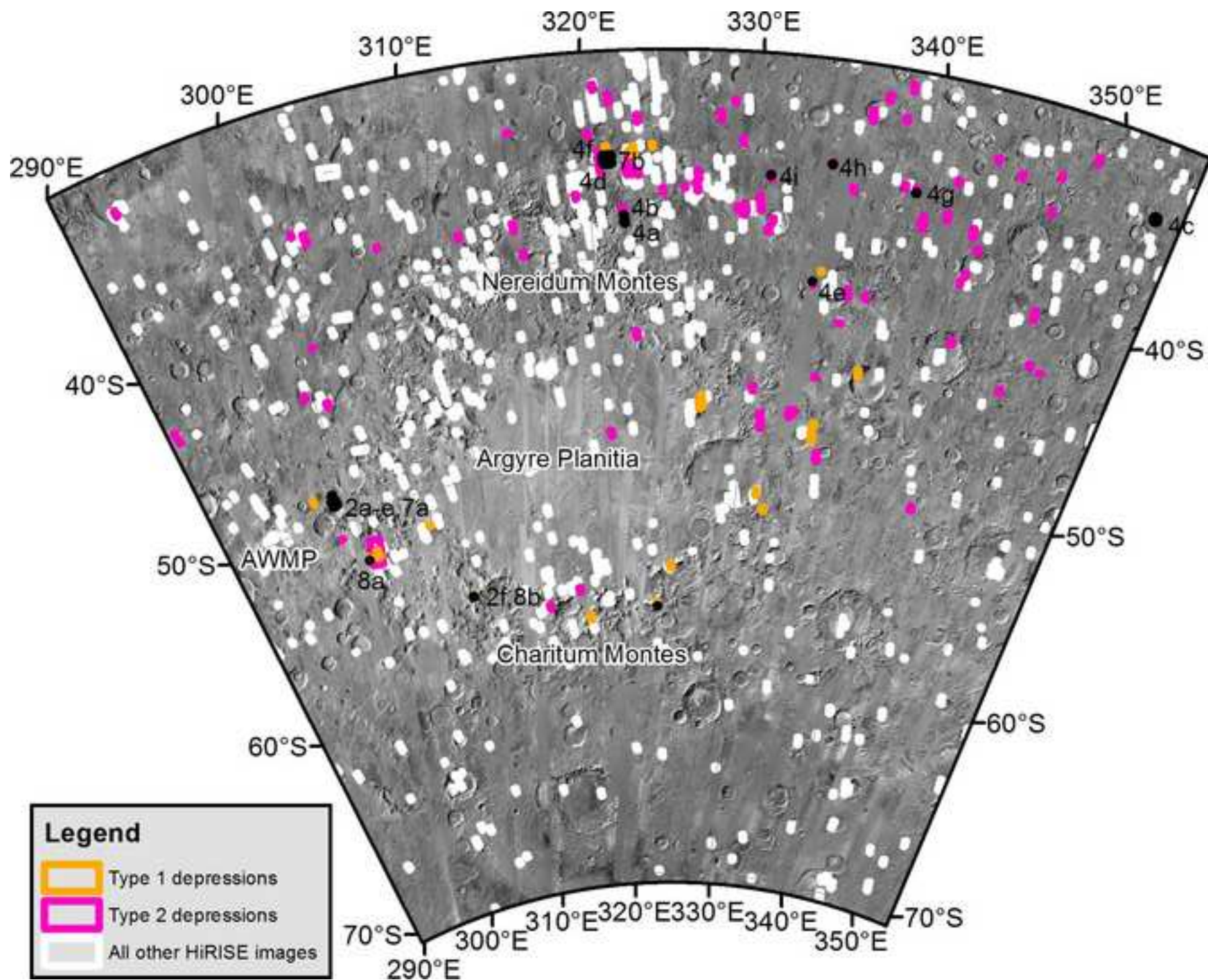
Figure



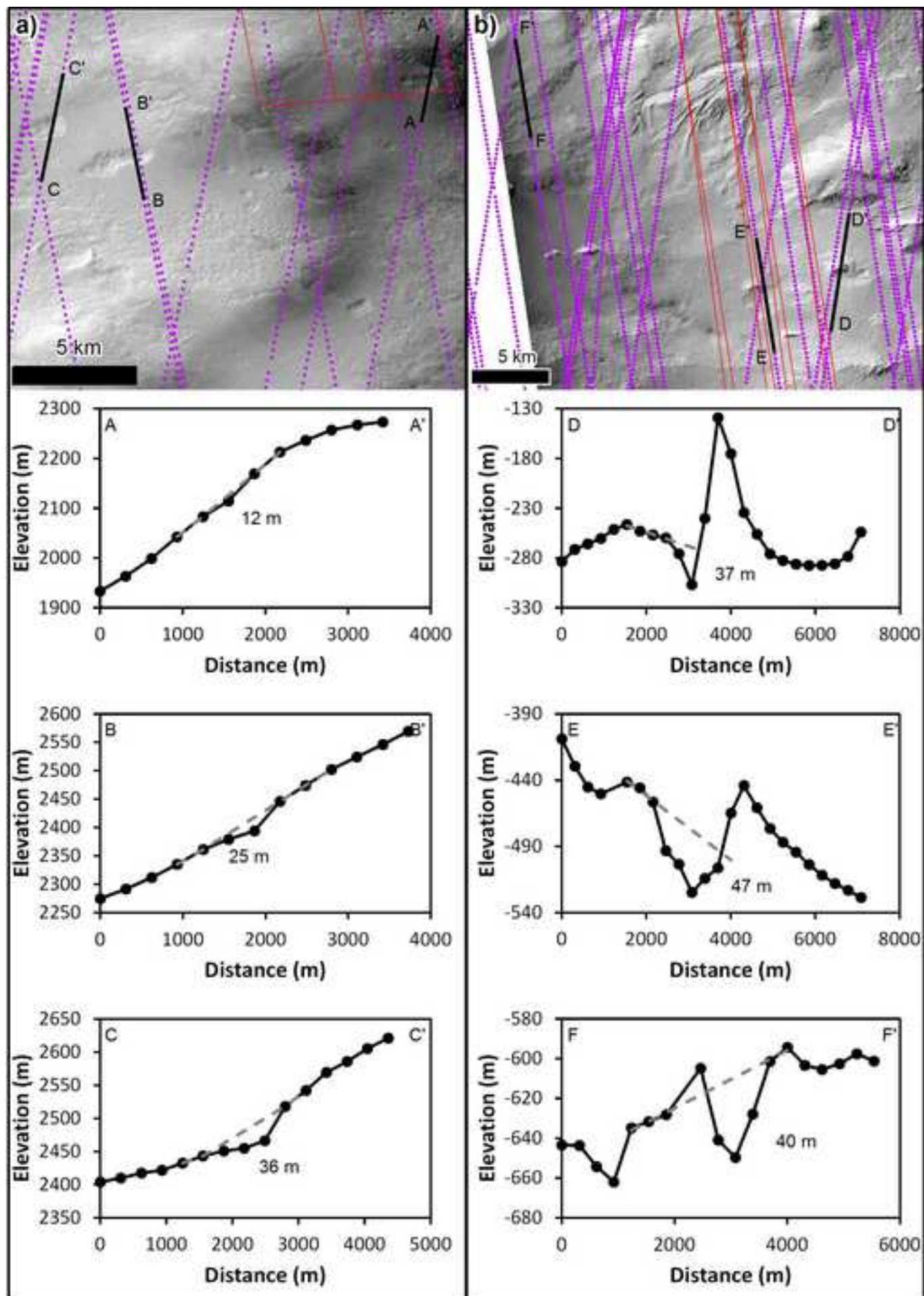
Figure



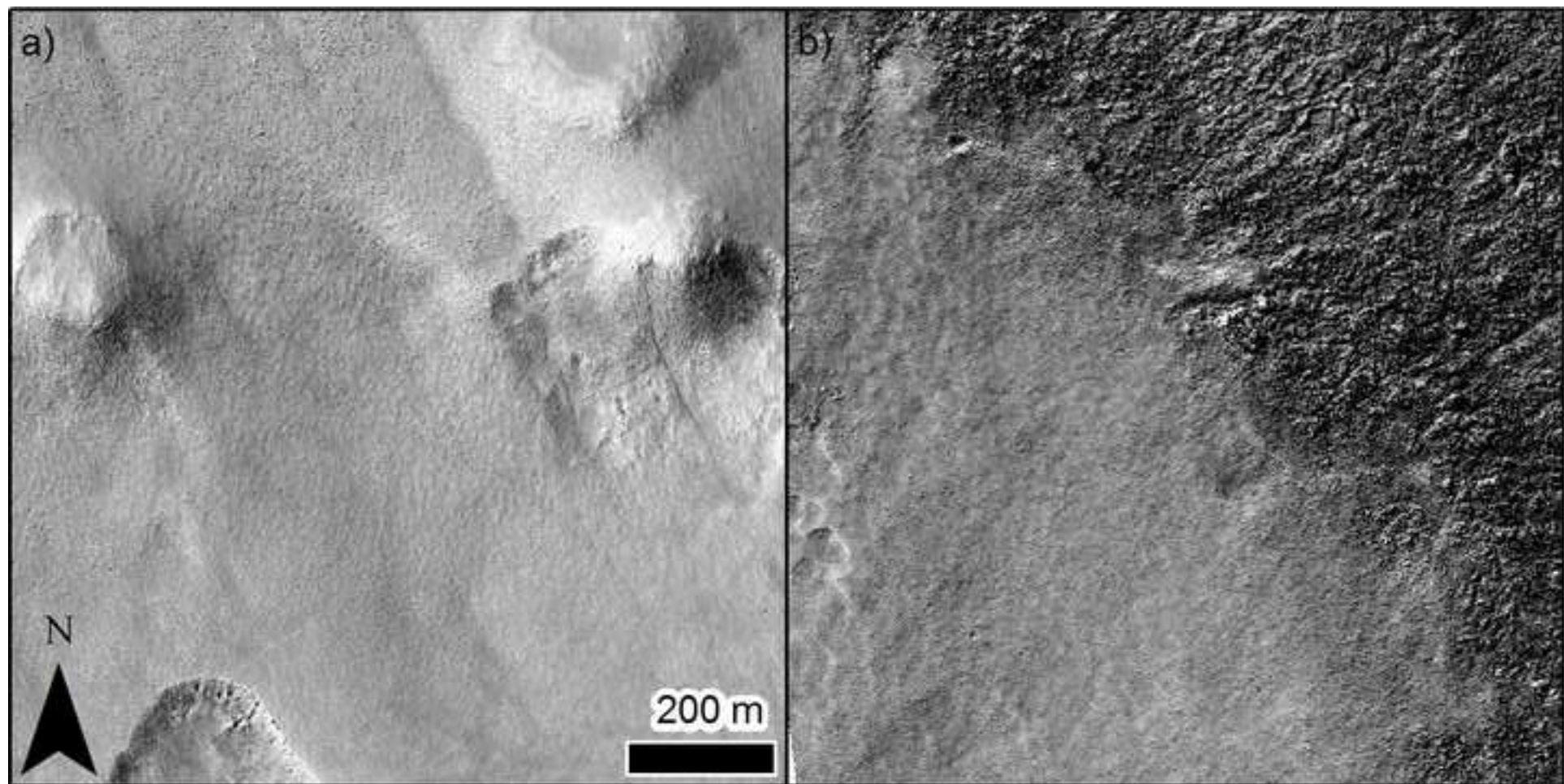
Figure



Figure



Figure



Figure

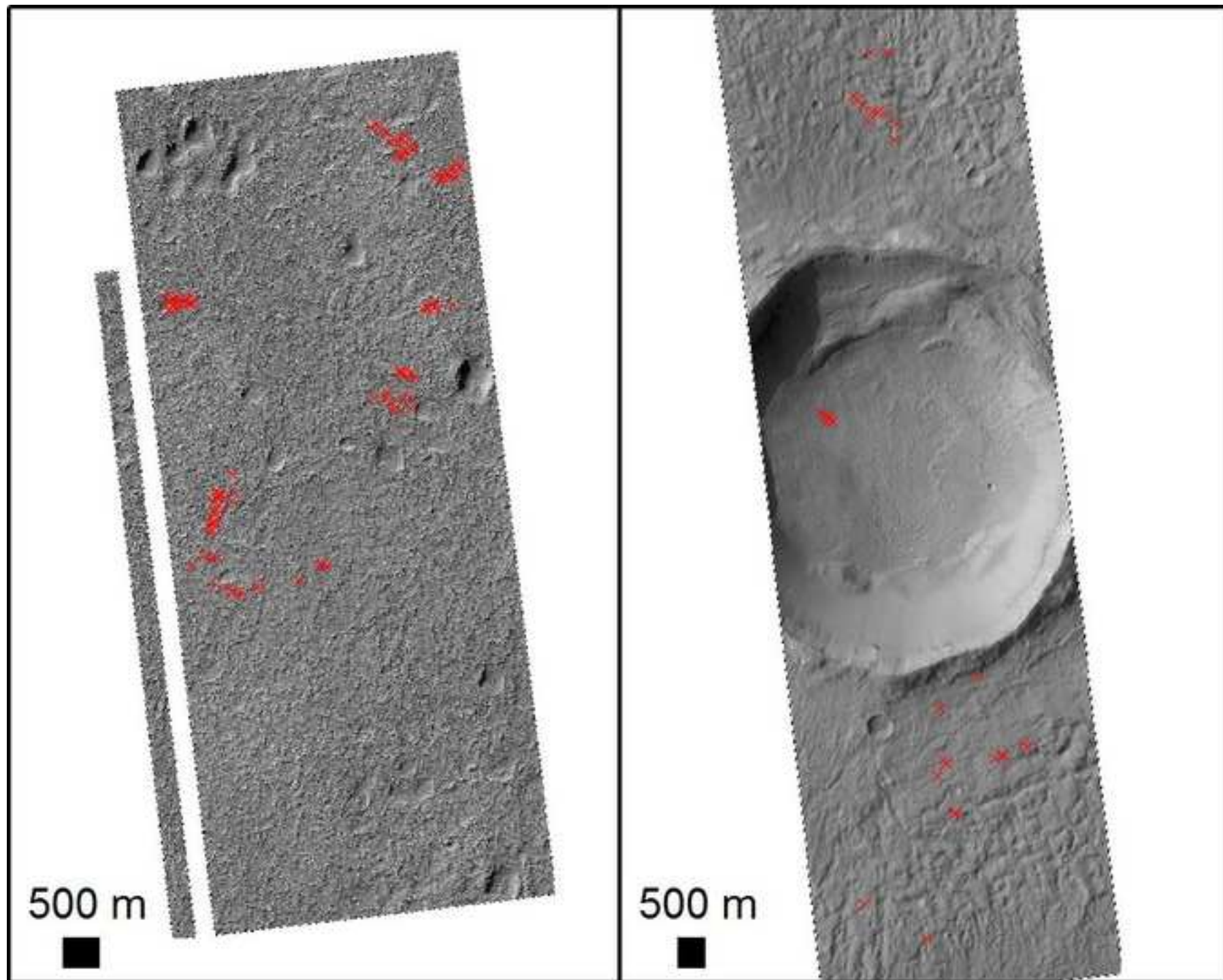


Table 1: Location and details of sites identified as having Type 1 depressions in this study.^a

Image #	Location	Site	Image reference	cm/pixel	longitude	latitude	Gullies	Polygons	Unit(s)	Unit Name(s)
1	1		ESP_039392_1450	25	323.816	34.588	x	x	C1	Old crater materials
2	2		PSP_004976_1450	50	322.723	34.797	x	x	C1	Old crater materials
3	3	(a)	ESP_012874_1450	25	322.526	34.869	x	x	C1	Old crater materials
4		(b)	ESP_013019_1450	25	322.525	34.872	x	x	C1	Old crater materials
5	4	(a)	PSP_007033_1445	50	321.183	35.000		x	Nabr (and Nh2 in northernmost 10%, Cr in very SE)	Argyre basin and rim materials
6		(b)	ESP_016197_1445	50	321.184	35.004		x	Nabr (and Nh2 in northernmost 10%, Cr in very SE)	Argyre basin and rim materials
7	5		ESP_040974_1395	25	334.513	40.255	x	x	C1	Old crater materials
8	6		ESP_038521_1345	50	337.943	44.975		x	Cr and Cfs	Old crater materials and Smooth crater floor materials
9	7		PSP_006901_1325	50	327.104	47.078		x	NArb	Argye rim and basin materials
10	8		ESP_034829_1325	50	326.933	47.304	x	x	NArb	Argye rim and basin materials
11	9		ESP_034829_1325	50	326.933	47.304	x	x	NArb	Argye rim and basin materials
12	10		PSP_006993_1320	25	335.384	47.804	x	x	NABr	Argyre basin and rim materials
13	11		PSP_002457_1310	25	335.305	48.208	x	x	NABr	Argyre basin and rim materials
14	12		ESP_011911_1310	50	335.371	48.533	x	x	NABr	Argyre basin and rim materials
15	13		PSP_001349_1310	50	335.336	48.578	x	x	NABr	Argyre basin and rim materials
16	14		ESP_023925_1305	25	297.495	48.851		x	Nh1 and Hnb	Highlands member 1 and Highlands basins materials
17	15		ESP_011319_1305	50	298.954	49.001		x	Nh1	Highlands member 1
18	16		ESP_039049_1280	25	331.610	51.484	x	x	C2	Young crater materials
19	17		ESP_021960_1280	25	305.499	51.706		x	C1	Old crater materials
20	18		ESP_038640_1275	25	332.262	52.267	x	x	C2	Young crater materials
21	19	(a)	PSP_003711_1275	25	300.895	52.312		x	NAb1, NArb, NAr	Argyre basin member 1, Argye rim and basin materials, Argye rim materials
22		(b)	PSP_005333_1275	25	300.902	52.324		x	NAb1, NArb, NAr	Argyre basin member 1, Argye rim and basin materials, Argye rim materials
23	20	(a)	ESP_032628_1275	25	300.048	52.398		x	NAb1, NArb, NAr	Argyre basin member 1, Argye rim and basin materials, Argye rim materials
24		(b)	ESP_032773_1275	25	300.049	52.399		x	NAb1, NArb, NAr	Argyre basin member 1, Argye rim and basin materials, Argye rim materials
25	21		PSP_003922_1275	25	300.755	52.411	x	x	NAb1, NArb, NAr	Argyre basin member 1, Argye rim and basin materials, Argye rim materials
26	22		PSP_005319_1245	25	324.839	55.273	x	x	NAr	Argyre rim materials
27	23		ESP_013890_1240	50	307.523	55.615		x	NABr, NAr	Argyre basin and rim materials, Argye rim materials
28	24		PSP_006176_1225	25	323.637	57.130		x	NArb	Argye rim and basin materials
29	25		PSP_002761_1220	25	317.578	57.610		x	NArb, NAb2, NAb3	Argyre rim and basin materials, Argyre basin member 2, Argyre basin member 3

^a"x" means the feature is present.

Table 2: Location and details of sites identified as having Type 2 depressions in this study.^a

Image #	Location	Site	Image reference	cm/pixel	longitude	latitude	Gullies	Polygons
1	1	(a)	ESP_023396_1490	50	338.302	30.832	x	
2		(b)	ESP_024319_1490	50	338.300	30.834	x	
3	2	(a)	PSP_008153_1480	50	337.094	31.475	x	
4		(b)	PSP_009155_1480	50	337.095	31.475	x	
5		(c)	ESP_021695_1480	25	337.094	31.457	x	
6		(d)	ESP_022684_1480	50	337.096	31.485	x	
7	3		ESP_020232_1480	50	320.528	31.687	x	
8	4		ESP_017330_1475	50	349.176	31.991	x	
9	5		ESP_025758_1475	50	293.004	32.064		
10	6		ESP_027247_1470	50	321.371	32.249		
11	7	(a)	ESP_022895_1475	25	338.199	32.321	x	
12		(b)	ESP_022262_1475	25	338.199	32.322	x	
13	8	(a)	ESP_039286_1480	25	337.091	31.469	x	
14		(b)	ESP_027075_1475	25	338.194	32.348	x	
15		(c)	ESP_027774_1475	25	338.195	32.350	x	
16		(d)	ESP_038112_1475	25	338.196	32.350	x	
17		(e)	ESP_036345_1475	50	338.196	32.352	x	
18		(f)	ESP_031954_1475	25	338.204	32.354	x	
19		(g)	ESP_035501_1475	25	338.197	32.353	x	
20		(h)	ESP_037057_1475	50	338.198	32.356	x	
21		(i)	ESP_030820_1475	25	338.205	32.357	x	
22		(j)	ESP_032165_1475	25	338.205	32.358	x	
23		(k)	ESP_013836_1475	25	338.193	32.360	x	
24	9		PSP_008364_1475	50	336.325	32.433		
25	10		PSP_007916_1475	50	328.560	32.412		
26	11		ESP_034908_1465	50	327.791	33.121		
27	12	(a)	PSP_006756_1465	25	322.972	33.257		
28		(b)	ESP_023779_1465	25	322.977	33.263		
29	13		ESP_016262_1465	25	347.469	33.263	x	
31	14		ESP_028776_1465	25	343.720	33.324	x	
32	15		ESP_026733_1460	25	315.544	33.524		
33	16		ESP_021734_1460	25	353.240	33.752	x	
34	17		ESP_025466_1460	50	345.292	33.788		
35	18		ESP_034816_1460	50	320.094	33.966		
36	19	(a)	ESP_013098_1455	25	329.129	34.293	x	
37		(b)	PSP_004145_1455	25	329.123	34.305	x	
38	20		PSP_005806_1450	25	341.814	34.792		
39	21		ESP_028645_1450	50	320.647	34.882		
40	22		ESP_026851_1445	25	334.395	35.002		
41	23		ESP_017040_1445	50	347.511	35.017		
42	24		PSP_008114_1445	50	322.404	35.404	x	
43			ESP_017331_1440	50	322.647	35.730	x	
44	25		PSP_007679_1440	50	320.695	35.438		
45	26		PSP_007652_1440	25	338.813	35.540	x	

Image #	Location	Site	Image reference	cm/pixel	longitude	latitude	Gullies	Polygons
46	27		ESP_028552_1440	50	339.485	35.640	x	
48	28	(a)	ESP_022315_1440	25	330.846	35.843	x	
49		(b)	ESP_028038_1440	50	330.859	35.874	x	
50		(c)	ESP_036187_1440	50	330.858	35.875	x	
51		(d)	ESP_030517_1440	25	330.859	35.877	x	
52		(e)	ESP_028315_1440	25	330.860	35.879	x	
53	29	(a)	PSP_007468_1440	25	322.285	35.714	x	
54		(b)	PSP_006822_1440	25	322.285	35.720	x	
55	30		ESP_020166_1440	25	322.988	35.898		
56	31		PSP_008628_1435	50	326.543	35.986		
57	32		ESP_017436_1435	50	335.806	36.075		
58	33		ESP_030083_1435	50	301.948	36.084	x	
59	34		ESP_016501_1430	50	302.683	36.455	x	
60	35		ESP_025704_1430	50	326.490	36.555		
61	36		ESP_017594_1430	50	341.608	36.560	x	
62	37		PSP_010118_1430	50	325.712	36.581		
63	38		ESP_039115_1430	25	325.719	36.583		
64	39		ESP_040948_1430	25	324.416	36.738		
65	40		ESP_034104_1430	50	319.155	36.893		
66	41	(a)	ESP_015959_1425	25	340.227	37.010	x	
67		(b)	ESP_020706_1425	25	340.236	37.020	x	
68		(c)	PSP_007441_1425	50	340.232	37.098	x	
69	42		ESP_031176_1425	50	340.069	37.126	x	
70	43	(a)	PSP_006663_1425	25	343.355	37.034	x	
71		(b)	ESP_011436_1425	25	343.353	37.353	x	
72	44	(a)	ESP_039616_1420	25	329.319	37.535	x	?
73		(b)	ESP_039682_1420	25	329.316	37.524	x	?
74	45	(a)	ESP_025638_1425	50	330.327	37.195	x	
75		(b)	ESP_035264_1420	50	329.452	37.498	x	
76		(c)	ESP_026983_1420	50	329.451	37.516	x	
77		(d)	ESP_034341_1420	50	328.989	37.546	x	
78	46	(a)	ESP_016711_1420	50	329.360	37.610	x	
79		(b)	PSP_007771_1420	50	329.355	37.644	x	
80	47		ESP_013824_1420	25	306.731	37.801	x	
81	48		ESP_028420_1420	50	343.841	37.809		
82	49		PSP_007824_1420	50	322.026	37.895		
83	50		ESP_016078_1415	25	331.163	37.992	x	
84	51		ESP_026377_1415	50	315.180	38.081		
85	52		ESP_019995_1415	50	311.740	38.142		
86	53		ESP_038231_1410	50	330.955	38.513	x	
87	54		ESP_029765_1405	25	343.502	39.119		x
88	55		ESP_039721_1400	25	343.302	39.558	x	
89	56		PSP_008022_1405	50	315.598	39.425	x	
90	57		ESP_016829_1395	50	348.397	40.082		
91	58		ESP_040974_1395	25	334.513	40.255	x	x
92	59		ESP_038785_1390	25	334.041	40.881	x	?

Image #	Location	Site	Image reference	cm/pixel	longitude	latitude	Gullies	Polygons
93	60		ESP_029462_1385	50	336.370	41.136		
94	61	(a)	ESP_029963_1385	25	337.550	41.202	x	
95		(b)	ESP_030596_1385	25	337.554	41.212	x	
96	62		ESP_016211_1380	25	301.066	41.610	x	
97	63		ESP_016038_1370	25	343.722	42.478		
98	64		ESP_027167_1370	50	349.113	42.515		
99	65		ESP_041013_1370	25	349.907	42.657	x	
100	66	(a)	ESP_032086_1370	25	336.126	42.652	x	
101		(b)	ESP_032653_1370	25	336.155	42.658	x	
102	67		ESP_021855_1365	50	290.478	43.200		
103	68		ESP_037084_1360	50	322.576	43.780	x	
104	69		ESP_028514_1360	50	299.475	43.815		
105	70		PSP_004118_1355	25	347.701	44.138	x	
106	71		ESP_036887_1350	50	300.830	44.526		
107	72		ESP_032152_1340	25	335.015	45.473		
108	73		ESP_025071_1335	50	330.711	46.311		
109	74		ESP_034829_1325	50	326.933	47.304	x	
110	75	(a)	ESP_038917_1325	25	333.794	47.311	x	
111		(b)	ESP_029950_1325	25	333.483	47.399	x	
112	76		ESP_015933_1320	50	331.427	47.894		
113	77		ESP_032825_1310	25	320.439	48.617		
114	78	(a)	ESP_033299_1305	50	335.893	49.351		
115		(b)	ESP_024372_1305	50	335.910	49.345		
116	79		ESP_023475_1285	50	343.847	50.947		x
117	80		ESP_013587_1285	25	298.573	51.052		
118	81		AEB_000001_0150	25	300.769	52.203		
119	82	(a)	ESP_012848_1235	25	316.839	56.211		
120		(b)	ESP_012782_1235	25	316.838	56.218		
121	83		ESP_032377_1230	50	314.042	56.867		

^{a)}“x” means the feature is present and “?” means uncertain.